THE ASTROPHYSICAL JOURNAL, 533:424–439, 2000 April 10

GENERAL RELATIVISTIC EFFECTS ON NEUTRINO-DRIVEN WINDS FROM YOUNG, HOT NEUTRON STARS AND *r*-PROCESS NUCLEOSYNTHESIS

KAORI OTSUKI
Division of Theoretical Astrophysics, National Astronomical Observatory, Mitaka, Tokyo 181-8588, Japan
HIDEYUKI TAGOSHI
Department of Earth and Space Science, Osaka University, Toyonaka, Osaka 560-0043, Japan
AND
TOSHITAKA KAJINO[1,2] AND SHIN-YA WANAJO
Division of Theoretical Astrophysics, National Astronomical Observatory, Mitaka, Tokyo 181-8588, Japan
Received 1999 March 21; accepted 1999 November 3

ABSTRACT

Neutrino-driven winds from young hot neutron stars, which are formed by supernova explosions, are the most promising candidate site for *r*-process nucleosynthesis. We study general relativistic effects on this wind in Schwarzschild geometry in order to look for suitable conditions for successful *r*-process nucleosynthesis. It is quantitatively demonstrated that general relativistic effects play a significant role in increasing the entropy and decreasing the dynamic timescale of the neutrino-driven wind. Exploring the wide parameter region that determines the expansion dynamics of the wind, we find interesting physical conditions that lead to successful *r*-process nucleosynthesis. The conditions that we found are realized in a neutrino-driven wind with a very short dynamic timescale, $\tau_{\rm dyn} \sim 6$ ms, and a relatively low entropy, $S \sim 140$. We carry out α-process and *r*-process nucleosynthesis calculations on these conditions with our single network code, which includes over 3000 isotopes, and confirm quantitatively that the second and third *r*-process abundance peaks are produced in neutrino-driven winds.

Subject headings: nuclear reactions, nucleosynthesis, abundances — relativity — stars: neutron — stars: winds, outflows — supernovae: general

1. INTRODUCTION

The *r*-process is a nucleosynthesis process that produces elements heavier than iron (Burbidge et al. 1957). They make up nearly half of the massive nuclear species and show typical abundance peaks around nuclear masses $A = 80$, 130, and 195, at which neutron numbers are slightly smaller than the magic numbers $N = 50$, 82, and 126, respectively. This fact suggests that the *r*-process elements have completely a different origin than the *s*-process elements, whose abundance peaks are located just on the neutron magic numbers. The *r*-process elements are presumed to be produced in an explosive environment with short timescale and high entropy, where an intensive flux of free neutrons is absorbed by seed elements successively to form the nuclear reaction flow on extremely unstable nuclei on the neutron-rich side. Recent progress in studies of the nuclear physics of unstable nuclei has made it possible to simulate *r*-process nucleosynthesis by the use of the accumulated knowledge of the nuclear masses and beta half-lives of several critical radioactive elements.

The studies of *r*-process elements also have an effect on the cosmic age problem, that is, that the age of the universe as derived from cosmological constants and the age of the oldest globular cluster conflict. A typical *r*-process element, thorium, has been detected recently in very metal-deficient stars, providing an independent method to estimate the age of the Milky Way Galaxy (Sneden et al. 1996). Since thorium has a half-life of 14 Gyr, the observed abundance relative to other stable elements is used as a chronometer for dating the age of the Galaxy. To study the origin of the *r*-process elements is thus important and even critical in order to understand the cosmology and astronomy of Galactic chemical evolution and the nuclear physics of unstable nuclei. Unfortunately, however, the astrophysical site of the *r*-process nucleosynthesis has been poorly known, although several candidate sites are proposed and are being investigated theoretically.

The neutrino-driven wind, the subject of this study, is thought to be one of the most promising candidates for the site of *r*-process nucleosynthesis. It is generally believed that a neutron star is formed as the remnant of the gravitational core collapse of a Type II, Ib, or Ic supernova. The hot neutron star just born releases most of its energy as neutrinos during the Kelvin-Helmholtz cooling phase, and these neutrinos drive matter outflow from the surface. This outflow is called the neutrino-driven wind. Many theoretical studies of the neutrino-driven wind followed the successful detection of energetic neutrinos from SN 1987A, which raised the possibility of finding *r*-process nucleosynthesis in this wind.

Although there are several numerical simulations of the neutrino-driven wind, their results vary significantly depending on the models and methods adopted (Woosley et al. 1994; Witti, Janka, & Takahashi 1994; Takahashi, Witti, & Janka 1994). A benchmark study of numerical simulations by Wilson and his collaborators (Woosley et al. 1994) has successfully explained the solar system *r*-process abundances, but the other studies mentioned above (Witti et al. 1994; Takahashi et al. 1994; Takahashi & Janka 1996) have not been able to reproduce their result. Qian & Woosley (1996) tried to work out this discrepancy by using approx-

[1] Department of Astronomy, University of Tokyo, Hongo, Tokyo 113-0033, Japan.
[2] Department of Astronomical Science, Graduate University for Advanced Studies, Mitaka, Tokyo 181-8588, Japan.

imate methods to solve the spherically symmetric, steady state flow in the Newtonian framework.

They could not find suitable conditions for r-process nucleosynthesis, and they suggested in a post-Newtonian calculation that general relativistic effects may improve thermodynamic conditions for r-process nucleosynthesis. Cardall & Fuller (1997) adopted similar approximate methods in a general relativistic framework and obtained a short dynamic timescale of expansion and a large entropy, which is in reasonable agreement with the result of the post-Newtonian approximation adopted by Qian & Woosley (1996). They did not specify, however, what kind of specific effect among several general relativistic effects is responsible for this change.

Since the wind blows near the surface of a neutron star, it is necessary to study the expansion dynamics of the neutrino-driven wind in general relativity. The first purpose of this paper is to make clear quantitatively the effects of general relativity by adopting a fully general-relativistic framework. Although we assume only a spherical steady state flow of the neutrino-driven wind, we do not adopt approximate methods as in several previous studies. We try to extract wind properties as general as possible in supernova-independent models in order to allow comparison with the expansion of different objects, such as the accretion disk of a binary neutron star merger (Symbalisty & Schramm 1982) or a subcritical low-mass neutron star (Sumiyoshi et al. 1998), which would be induced by an intense neutrino burst. The second purpose is to look for conditions suitable for the r-process. The key quantities needed to explain the solar system r-process abundances are the mass outflow rate $\dot{M}$, the dynamic timescale of expansion $\tau_{\rm dyn}$, the entropy S, and the electron fraction Y_e. The third purpose of this paper is to make clear how these thermodynamic and hydrodynamic quantities affect r-process nucleosynthesis by carrying out the nucleosynthesis calculation numerically.

In the next section we explain our theoretical models of the neutrino-driven wind. We introduce basic equations to describe the dynamics of the wind in the Schwarzschild geometry. Boundary conditions and adopted parameters for solving these equations are presented in this section. Numerical results are shown in § 3, where the effects of general relativity are studied in detail. We also investigate the dependence of the key physical quantities like $\tau_{\rm dyn}$ and S on the neutron star mass, radius, and neutrino luminosity in order to look for neutrino-driven wind conditions that are suitable for r-process nucleosynthesis. Applying the result obtained in § 3, we carry out the nucleosynthesis calculation in § 4. The purpose of this section is to confirm quantitatively that r-process elements are produced successfully in a wind with a very short dynamic timescale and relatively low entropy. We finally summarize the results of this paper and present further discussions and the outlook for future research in § 5.

2. MODELS OF NEUTRINO-DRIVEN WINDS

2.1. *Basic Equations*

A Type II or Ib supernova explosion is a complex hydrodynamic process that needs careful theoretical studies of the convection associated with shock propagation. Our time of interest, however, is the later phase after the core bounce at which the shock has already passed, reaching a radius about 10,000 km, and continuous mass outflow from the surface of the neutron star has begun. A recent three-dimensional numerical simulation (Hillebrandt 1999) has shown that the convection near the shock front does not grow as deep as two-dimensional numerical simulations have indicated and that the hydrodynamic conditions behind the shock are more likely similar to those obtained in one-dimensional numerical simulations. Since Wilson's numerical simulation of SN 1987A in Woosley et al. (1994) has shown that the neutrino-driven wind is adequately described by a steady state flow, we here adopt a spherically symmetric, steady state wind, following previous studies (Duncan, Shapiro, & Wasserman 1986; Qian & Woosley 1996; Cardall & Fuller 1997). According to Wilson's numerical simulation, the neutrino luminosity L_ν changes slowly from about 10^{52} ergs s^{-1} to below 10^{51} ergs s^{-1} during ~ 10 s of the Kelvin-Helmholtz cooling phase of the neutron star. The properties of the proto–neutron star, i.e., the mass M and radius R, also evolve slowly. We therefore take these quantities, L_ν, M, and R, as input parameters in order to describe more rapid evolution of the neutrino-driven wind.

The basic equations to describe the spherically symmetric, steady state winds in the Schwarzschild geometry are (Shapiro & Teukolsky 1983)

$$\dot{M} = 4\pi r^2 \rho_b u \,, \tag{1}$$

$$u \frac{du}{dr} = \frac{1}{\rho_{\rm tot} + P} \frac{dP}{dr} \left(1 + u^2 - \frac{2M}{r}\right) - \frac{M}{r^2} \,, \tag{2}$$

and

$$\dot{q} = u\left(\frac{d\varepsilon}{dr} - \frac{P}{\rho_b^2} \frac{d\rho_b}{dr}\right) , \tag{3}$$

where $\dot{M}$ is the mass outflow rate, r is the distance from the center of the neutron star, ρ_b is the baryon mass density, u is the radial component of the four-velocity, $\rho_{\rm tot} = \rho_b + \rho_b \varepsilon$ is the total energy density, ε is the specific internal energy, P is the pressure, M is the mass of the neutron star, and $\dot{q}$ is the net heating rate due to neutrino interactions with matter. We use the conventional units in which the Planck constant $\hbar$, the speed of light c, the Boltzmann constant k, and gravitational constant G, are taken to be unity. Because the neutrino-driven wind blows from the surface of the hot proto–neutron star at a high temperature, $T \sim 5$ MeV, and also because the physics of the wind is mostly determined at $T \gtrsim 0.5$ MeV (Qian & Woosley 1996), the equations of state are approximately written as

$$P = \frac{11\pi^2}{180} T^4 + \frac{\rho_b}{m_N} T \,, \tag{4}$$

$$\varepsilon = \frac{11\pi^2}{60} \frac{T^4}{\rho_b} + \frac{3}{2} \frac{T}{m_N} \,, \tag{5}$$

where T is the temperature of the system and m_N is the nucleon rest mass. We have assumed that the material in the wind consists of photons, relativistic electrons and positrons, and nonrelativistic free nucleons.

The heating rate $\dot{q}$ in equation (3) through the interactions between neutrinos and matter is the key to understanding the dynamics of the neutrino-driven wind.

Following Bethe (1993), Bethe et al. (1980), and Qian & Woosley (1994), we take account of the following five neutrino processes: three heating processes, neutrino and antineutrino absorption by free nucleons, neutrino and antineutrino scattering by electrons and positrons, and neutrino-antineutrino annihilation into electron-positron pairs; and two cooling processes, electron and positron capture by free nucleons and electron-positron annihilation into neutrino-antineutrino pairs. We assume that neutrinos are emitted isotropically from the surface of the neutron star at radius R, which has proven to be a good approximation in recent numerical studies of neutrino transfer (Yamada, Janka, & Suzuki 1999). In this paper, therefore, we make the assumption that the neutrinosphere radius is equal to the proto–neutron star radius: $R_\nu = R$. Since the neutrino trajectory is bent in the Schwarzschild geometry, the material in the wind sees neutrinos within the solid angle subtended by the neutrinosphere, which is greater than the solid angle in the Newtonian geometry at the same coordinate radius. The bending effect of the neutrino trajectory increases the heating rate compared to the Newtonian case. We also have to take account of the effect of redshift on the neutrino energy, which tends to decrease the heating rate.

The important heating rate is due to neutrino and antineutrino absorption by free nucleons,

$$\nu_e + n \rightarrow p + e^- \tag{6}$$

and

$$\bar{\nu}_e + p \rightarrow n + e^+ , \tag{7}$$

and it is given by

$$\dot{q}_1 \approx 9.65 N_{\rm A}[(1 - Y_e) L_{\nu_e,51}\, \varepsilon_{\nu_e}^2 + Y_e\, L_{\bar{\nu}_e,51}\, \varepsilon_{\bar{\nu}_e}^2] \times \frac{1 - g_1(r)}{R_{\nu 6}^2}\, \Phi(r)^6 \ {\rm MeV\ s^{-1}\ g^{-1}} , \tag{8}$$

where the first and second terms in parentheses are for the processes given in equations (6) and (7), respectively; ε_i is the energy in MeV defined by $\varepsilon_i = (\langle E_i^3\rangle/\langle E_i\rangle)^{1/2}$; and $\langle E_i^n\rangle$ denotes the nth energy moment of the neutrino ($i = \nu_e$) and antineutrino ($i = \bar{\nu}_e$) energy distribution, $N_{\rm A}$ is the Avogadro number, Y_e is the electron fraction, $L_{i,51}$ is the individual neutrino or antineutrino luminosity in units of 10^{51} ergs s^{-1}, and $R_{\nu 6}$ is the neutrinosphere radius in units of 10^6 cm. In this equation, $1 - g_1(r)$ is the geometrical factor that represents the effect of bending neutrino trajectory and $g_1(r)$ is given by

$$g_1(r) = \left[1 - \left(\frac{R_\nu}{r}\right)^2 \frac{1 - 2M/r}{1 - 2M/R_\nu}\right]^{1/2} , \tag{9}$$

where the function $(1 - 2M/r)/(1 - 2M/R_\nu)$ arises because of the Schwarzschild geometry—unity should be substituted for this factor in the Newtonian geometry. We also define the redshift factor

$$\Phi(r) = \sqrt{\frac{1 - 2M/R_\nu}{1 - 2M/r}} , \tag{10}$$

in the Schwarzschild geometry; this factor, too, should be unity in the Newtonian geometry. We will discuss the effects of these general relativistic correction factors in the next section.

The second heating rate, due to neutrino and antineutrino scattering by electrons and positrons, plays an equally important role. Neutrinos of all flavors can contribute to the scattering, and the heating rate is given by

$$\dot{q}_3 \approx 2.17 N_{\rm A}\, \frac{T_{\rm MeV}^4}{\rho_8} \left(L_{\nu_e,51}\, \epsilon_{\nu_e} + L_{\bar{\nu}_e,51}\, \epsilon_{\bar{\nu}_e} + \frac{6}{7}\, L_{\nu_\mu,51}\, \epsilon_{\nu_\mu}\right) \times \frac{1 - g_1(r)}{R_{\nu 6}^2}\, \Phi(r)^5 \ {\rm meV\ s^{-1}\ g^{-1}} , \tag{11}$$

where $\epsilon_i = \langle E_i^2\rangle/\langle E_i\rangle$ is in MeV ($i = \nu_e$, $\bar{\nu}_e$, and ν_μ) and we have assumed the same contribution from the ν_μ, $\bar{\nu}_\mu$, ν_τ, and $\bar{\nu}_\tau$ fluxes. We take $\varepsilon_i^2 \simeq 1.14\epsilon_i^2$ from the numerical studies by Qian & Woosley (1996).

The third heating rate, due to neutrino-antineutrino pair annihilation into electron-positron pairs, is given by

$$\dot{q}_5 \approx 12.0 N_{\rm A} \left[L_{\nu_e,51}\, L_{\bar{\nu}_e,51} (\epsilon_{\nu_e} + \epsilon_{\bar{\nu}_e}) + \frac{6}{7}\, L_{\nu_\mu,51}^2\, \epsilon_{\nu_\mu}\right] \times \frac{g_2(r)}{\rho_8\, R_{\nu 6}^4}\, \Phi(r)^9 \ {\rm meV\ s^{-1}\ g^{-1}} , \tag{12}$$

where $g_2(r)$ is given by

$$g_2(r) = [1 - g_1(r)]^4 [g_1(r)^2 + 4 g_1(r) + 5] . \tag{13}$$

The cooling rates that we included in the present calculations are for the inverse reactions of the two heating processes considered in equations (8) and (12). The first cooling rate, due to electron and positron captures by free nucleons, which are the inverse reactions of (6) and (7), is given by

$$\dot{q}_2 \approx 2.27 N_{\rm A}\, T_{\rm MeV}^6 \ {\rm meV\ s^{-1}\ g^{-1}} . \tag{14}$$

The second cooling rate, due to electron-positron pair annihilation into neutrino-antineutrino pairs of all flavors, which is the inverse reaction of equation (12), is given by

$$\dot{q}_4 \approx 0.144 N_{\rm A}\, \frac{T_{\rm MeV}^9}{\rho_8} \ {\rm meV\ s^{-1}\ g^{-1}} . \tag{15}$$

Combining the above five heating and cooling rates, we obtain the total net heating rate $\dot{q}$:

$$\dot{q} = \dot{q}_1 - \dot{q}_2 + \dot{q}_3 - \dot{q}_4 + \dot{q}_5 . \tag{16}$$

As we will discuss in the next section, the first three heating and cooling rates $\dot{q}_1$, $\dot{q}_2$, and $\dot{q}_3$ dominate over the contributions from $\dot{q}_4$ and $\dot{q}_5$.

2.2. *Boundary Conditions and Input Parameters*

We assume that the wind starts from the surface of the proto–neutron star at radius $r_i = R$ and temperature T_i. Near the neutrinosphere and the neutron star surface, both heating (mostly $\dot{q}_1$) and cooling (mostly $\dot{q}_2$) processes almost balance with each other because of very efficient neutrino interactions with matter. The system is thus in kinetic equilibrium (Burrows & Mazurek 1982) at high temperature and high density. The inner boundary temperature T_i is determined such that the net heating rate $\dot{q}$ becomes zero at this radius. We have confirmed quantitatively that a small change in T_i does not influence the calculated thermodynamic and hydrodynamic quantities of the neutrino-driven wind very much. We use the density $\rho(r_i) = 10^{10}$ g cm^{-3} at the inner boundary, taken from the result of Wilson's numerical simulation in Woosley et al. (1994).

The luminosity of each type of neutrino L_i ($i = \nu_e$, $\bar{\nu}_e$, ν_μ, $\bar{\nu}_\mu$, ν_τ, $\bar{\nu}_\tau$) is similar to that of each other type and changes from about 10^{52} to 10^{50} ergs s^{-1} very slowly over

~ 10 s (Woosley et al. 1994). We therefore take the common neutrino luminosity L_ν as a constant input parameter. In the heating and cooling rates, however, we use $\epsilon_{\nu_e} = 12$ MeV, $\epsilon_{\bar{\nu}_e} = 22$ MeV, and $\epsilon_\nu = \epsilon_{\bar{\nu}} = 34$ MeV as the values of the neutrino energies for the other flavors at $r_i = R$, as in Qian & Woosley (1996). We take the neutron star mass as a constant input parameter in the range $1.2\ M_\odot \le M \le 2.0\ M_\odot$.

The mass outflow rate $\dot{M}$ determines how much material is ejected by the neutrino-driven wind. In equations (1), (2), and (3), $\dot{M}$ is taken to be a constant value determined by the following outer boundary condition. In any delayed explosion model of Type II supernovae (Woosley et al. 1994; Witti et al. 1994; Takahashi et al. 1994), the shock wave moves away to a radius around 10,000 km above the neutron star surface at time $1\ \mathrm{s} \lesssim t$ after core bounce. As we stated in the previous subsection, the neutrino-driven wind is described fairly well by a steady state flow between the neutron star surface and the shock. From this observation, the typical temperature at the location of the shock wave can be used as an outer boundary condition. We impose the boundary condition only for subsonic solutions by choosing the value of $\dot{M} < \dot{M}_{\rm crit}$ such that $T = 0.1$ MeV at $r \simeq 10{,}000$ km, where $\dot{M}_{\rm crit}$ is the critical value for a supersonic solution. Given $\rho(r_i)$, equation (1) also determines the initial velocity at $r = r_i$ for each $\dot{M}$.

We explore here the effects of the assumed boundary condition and the mass outflow rate $\dot{M}$ on the results of the calculated quantities of neutrino-driven winds. We show in Figures 1*a* and 1*b* the fluid velocity and the temperature as functions of radius from the center of a neutron star for various $\dot{M}$, where the neutron star mass $M = 1.4\ M_\odot$ and the neutrino luminosity $L_{\nu_e} = 10^{51}$ ergs s^{-1}. Figures 2*a* and 2*b* are the same as Figures 1*a* and 1*b* but for $M = 2.0\ M_\odot$ and $L_{\nu_e} = 10^{52}$ ergs s^{-1}. Different values of $\dot{M}$ are listed in Table 1 with their respective calculated entropies and dynamic timescales. These figures indicate that both the velocity and the temperature profiles are very sensitive to the adopted $\dot{M}$ corresponding to different boundary conditions at $r = 10{,}000$ km. However, the entropies are more or less similar to one another, while exhibiting very different dynamic timescales.

TABLE 1

ENTROPY AND DYNAMIC TIMESCALE FOR DIFFERENT $\dot{M}$

Curve (from Fig. 1)	$\dot{M}$ ($10^{-6}\ M_\odot$ s^{-1})	Entropy (K)	$\tau_{\rm dyn}$ (s)
Neutron Star Mass 1.4 $M_\odot$, Neutrino Luminosity 10^{51} ergs s^{-1}			
$M_{\rm crit}$	5.2681	116	0.037171
1	5.2500	117	0.041304
2	5.1500	120	0.084335
3	5.0855	123	0.16455
4	5.0000	126	0.71569
5[a]	4.8000	135	...
Neutron Star Mass 2.0 $M_\odot$, Neutrino Luminosity 10^{52} ergs s^{-1}			
$M_{\rm crit}$	1.2459×10^2	138	0.00507
1	1.2450×10^2	138	0.00618
2	1.2400×10^2	139	0.01088
3	1.2250×10^2	141	0.08962
4	1.2150×10^2	143	2.6272
5[a]	1.1950×10^2	146	...

[a] Since the temperature in the fifth case for both $M = 1.4\ M_\odot$ and $M = 2.0\ M_\odot$ does not decrease to $T = 0.5/e$ MeV within 10,000 km, $\tau_{\rm dyn}$ is not defined (see Figs. 1*b* and 2*b*).

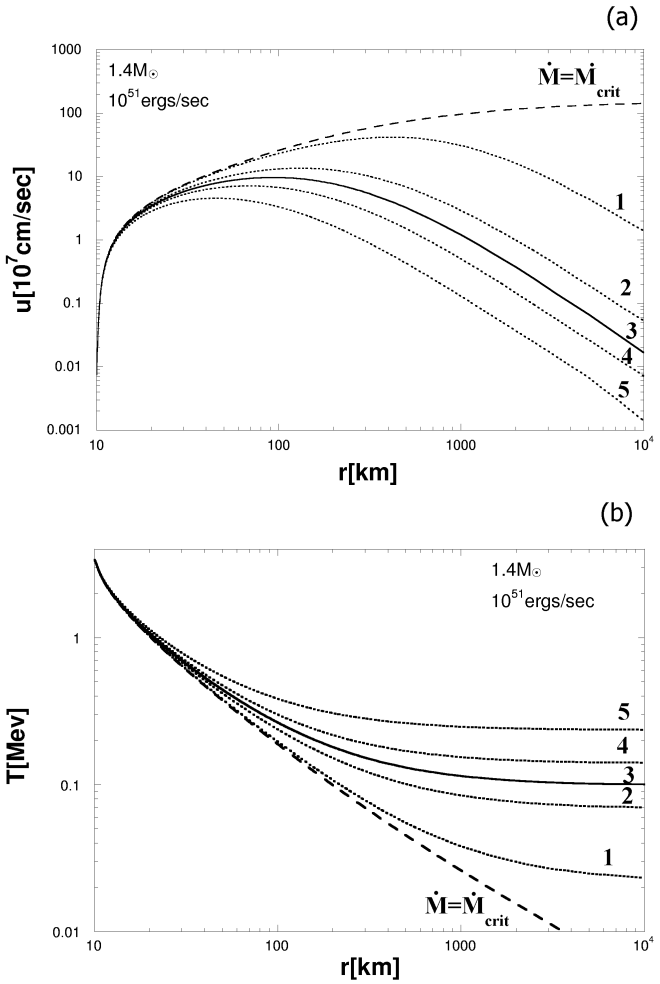

FIG. 1.—(*a*) Outflow velocity and (*b*) temperature in Schwarzschild geometry as a function of the distance r from the center of the neutron star for various mass outflow rates $\dot{M}$, where neutron star mass $M = 1.4\ M_\odot$ and neutrino luminosity $L_{\nu_e} = 10^{51}$ ergs s^{-1} are used. The long-dashed curve is for the critical mass outflow rate $\dot{M}_{\rm crit} = 5.2681 \times 10^{-6}\ M_\odot$, in which the velocity becomes supersonic through the critical point. Fives curves, numbered 1–5, correspond, respectively, to $\dot{M} = 5.25 \times 10^{-6}$, 5.15×10^{-6}, 5.0855×10^{-6}, 5.0×10^{-6}, and $4.8 \times 10^{-6}\ M_\odot$. The calculated result denoted "3" meets our imposed boundary condition of $T = 0.1$ MeV at $r = 10{,}000$ km. The entropy per baryon S and dynamic timescale $\tau_{\rm dyn}$ that correspond to each curve are tabulated in Table 1. Note that the temperature denoted by "5" does not decrease to $T = 0.5/e$ MeV within 10,000 km (see Table 1).

Although finding an appropriate boundary condition is not easy, it is one of the preferable manners of matching the conditions obtained in numerical simulations of a supernova explosion. We studied one of the successful simulations of a 20 $M_\odot$ supernova explosion assuming $M = 1.4\ M_\odot$ (J. R. Wilson 1998, private communication). Extensive studies of the *r*-process (Woosley et al. 1994) are based on his supernova model. Careful observation tells us that, although the neutrino luminosity for each flavor changes from 5×10^{52} ergs s^{-1} to 10^{50} ergs s^{-1}, the temperature decreases progressively to 0.1 MeV at around $r = 10{,}000$ km, where the shock front stays during the ~ 10 s after the core bounce at times that we are most interested in. It is to be noted that for *r*-process to be successful (Woosley et al. 1994) the temperature has to decrease gradually down

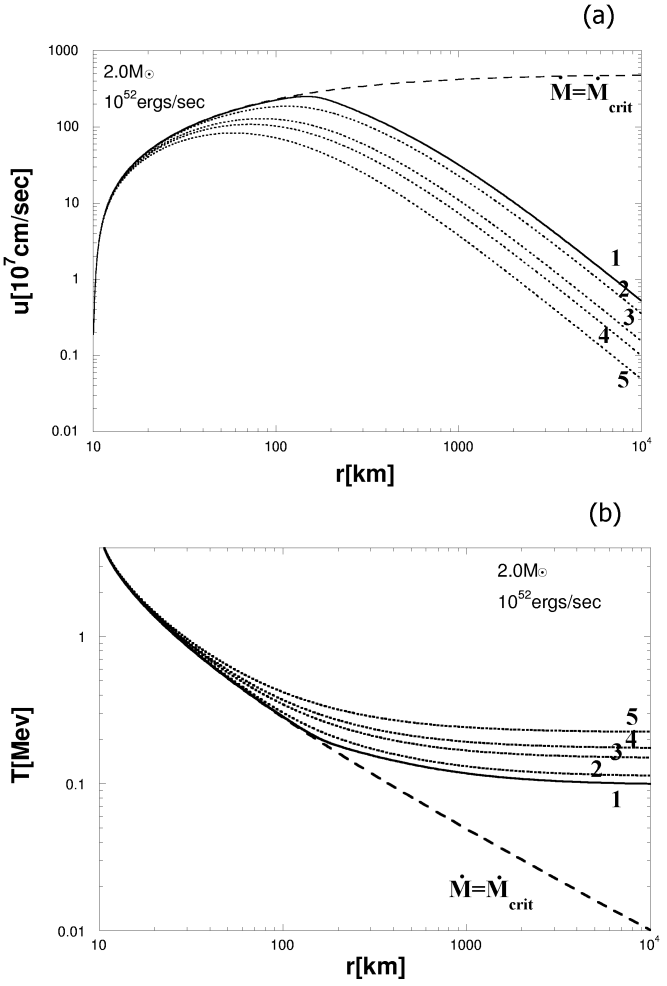

FIG. 2.—Same Fig. 1, but for the case of $M = 2.0\ M_\odot$, $L_{\nu_e} = 10^{52}$ ergs s^{-1}. The long-dashed curve is for the critical mass outflow rate $\dot{M}_{\rm crit} = 1.2459 \times 10^{-4}\ M_\odot$, and curves 1–5 correspond, respectively, to $\dot{M} = 1.245 \times 10^{-4}$, 1.240×10^{-4}, 1.225×10^{-4}, 1.215×10^{-4}, and $1.195 \times 10^{-4}\ M_\odot$. The calculated result denoted "1" meets our imposed boundary condition of $T = 0.1$ MeV at $r = 10{,}000$ km. The entropy per baryon S and the dynamic timescale $\tau_{\rm dyn}$ that correspond to each curve are shown in Table 1. Note that the temperature denoted by "5" does not decrease to $T = 0.5/e$ MeV within 10,000 km (see Table 1).

to around 0.1 MeV at the external region. This will be discussed in later sections. As displayed in Figures 1*a* and 1*b*, our calculation denoted by "3" meets this imposed boundary condition. Although it may not necessarily be clear, we can adopt the same boundary condition for the different neutron star masses that we study here, with the expectation that the physics continuously changes and with the aim of comparing the results that arise from the same boundary condition. Even in the case of a massive neutron star with $M = 2.0\ M_\odot$, as displayed in Figures 2*a* and 2*b*, we can still find a solution, denoted by "1" in the figures, that satisfies the same outer boundary condition. Although we found a solution with a reasonable value of $\dot{M}$, careful studies of numerical simulations of massive neutron stars are highly desirable in order to find a better boundary condition.

Let us discuss how our adopted outer boundary condition is not unreasonable. We are interested in the times $1\ {\rm s} \lesssim t$ when the neutrino-driven wind becomes quasi–steady state flow between the neutrinosphere and the shock front. The intense flux of neutrinos from the hot proto–neutron star has already interacted efficiently with radiation and relativistic electron-positron pairs at high temperature. Thus we have $T \sim T_\nu$, where T and T_ν are, respectively, the photon and neutrino temperatures. In this stage, the gain radius R_g (Bethe & Wilson 1985) at which the neutrino heating and cooling balance each other is very close to the neutrinosphere. Since we make the approximation that the neutrinosphere and the neutron star surface are similar, we here assume that the gain radius is also the same, i.e., $R_g = R_\nu = R$. On these conditions we can estimate the mass outflow rate $\dot{M}$ by considering the energy deposition to the gas from the main processes of neutrino capture on nucleons (eqs. [6] and [7]).

Following the discussion by Woosley et al. (1994), the rate of energy deposition in the gas above the neutrinosphere is given by

$$\dot{E} = (L_{\nu_e} + L_{\bar{\nu}_e}) \times \tau_\nu\ , \tag{17}$$

where τ_ν is the optical depth for the processes (6) and (7) and is given in terms of the opacity κ_ν and the pressure scale height L_p by

$$\begin{aligned}\tau_\nu &= \int_\infty^{R_g} \kappa_\nu \rho_b\, dr \\ &\approx \kappa_\nu(R_g)\rho_b(R_g)L_p(R_g) \\ &\approx 0.076 R_7^2 (T_\nu/3.5\ {\rm MeV})^6 (1.4\ M_\odot/M)\ . \end{aligned} \tag{18}$$

Note that $R_g = R$ and $T_\nu = T_i$. In order to obtain this expression, we have already used an approximate opacity (Bethe 1990; Woosley & Weaver 1993), $\kappa_\nu \approx 6.9 \times 10^{-18}(T_\nu/3.5\ {\rm MeV})^2\ {\rm cm}^2\ {\rm g}^{-1}$, and the pressure scale height in the radiation-dominated domain, which is written as

$$\begin{aligned} L_p &\approx (aT^4)/(GM\rho_b/R^2) \\ &= 74\ {\rm km}[(T\ {\rm MeV}^{-1})^4 R_7^2/\rho_{b,7}](1.4\ M_\odot/M)\ , \end{aligned} \tag{19}$$

where the subscripts on R_7 and $\rho_{b,7}$ indicate cgs multipliers in units of 10^7. The energy deposition equation (17) is mostly used for lifting the matter out of the gravitational well of the neutron star. Thus, inserting equation (18) into equation (17) and using the relation $L_{\nu_e} = L_{\bar{\nu}_e} = (7/4)\pi R^2 \sigma T_\nu^4$, the mass outflow rate $\dot{M}$ is approximately given by

$$\begin{aligned} \dot{M} &\approx \dot{E}/(GM/R) \\ &\approx 0.092[(L_{\nu_e} + L_{\bar{\nu}_e})/10^{53}\ {\rm ergs\ s^{-1}}]^{5/2} \\ &\quad \times (1.4\ M_\odot/M)^2\ M_\odot\ {\rm s}^{-1}\ . \end{aligned} \tag{20}$$

Our mass outflow rate $\dot{M}$ obtained from the imposed boundary condition of a temperature 0.1 MeV at 10,000 km is in reasonable agreement with the estimate from equation (20), to within a factor of 5 for 10^{50} ergs $s^{-1} \le (L_{\nu_e} + L_{\bar{\nu}_e}) \le 10^{52}$ ergs s^{-1}.

2.3. *Characteristics of the Neutrino-driven Wind*

When the material of the wind is on the surface of the neutron star and neutrinosphere, thermodynamic quantities still reflect the effects of neutralization, and the electron fraction Y_e remains as low as ~ 0.1. Once the wind leaves surface after the core bounce, electron number density decreases abruptly and the chemical equilibrium among leptons is determined by the balance between the two pro-

cesses (6) and (7) due to intense neutrino fluxes, shifting Y_e to ~ 0.5. An interesting phase for our purpose, studying the physical condition of the neutrino-driven wind suitable for r-process nucleosynthesis, starts when the temperature falls to $\sim 10^{10}$ K. At this temperature the material is still in nuclear statistical equilibrium (NSE) and the baryon numbers are carried by only free protons and neutrons. The neutron-to-proton number abundance ratio is determined by Y_e for charge neutrality.

Electron antineutrinos have a harder spectrum than electron neutrinos, as evident from their energy moments $\epsilon_{\nu_e} = 12$ MeV $< \epsilon_{\bar{\nu}_e} = 22$ MeV. Thus, the material is slightly shifted toward being neutron rich. Assuming weak equilibrium, this situation is approximately described by

$$Y_e \approx \frac{\lambda_{\nu_e n}}{\lambda_{\nu_e n} + \lambda_{\bar{\nu}_e p}} \approx \left(1 + \frac{L_{\bar{\nu}_e}}{L_{\nu_e}} \frac{\epsilon_{\bar{\nu}_e} - 2\delta + 1.2\delta^2/\epsilon_{\bar{\nu}_e}}{\epsilon_{\nu_e} + 2\delta + 1.2\delta^2/\epsilon_{\nu_e}}\right)^{-1}, \quad (21)$$

where $\lambda_{\nu_e n}$ and $\lambda_{\bar{\nu}_e p}$ are the reaction rates for processes (6) and (7), respectively, and δ is the neutron-proton mass difference (Qian & Woosley 1996). In our parameter set of neutron star mass $M = 1.4\ M_\odot$ and radius $R = 10$ km, for example, Y_e varies from $Y_e(r = R) = 0.43$ to $Y_e(r = 10{,}000$ km$) = 0.46$ very slowly because of the redshift factor (10) due to $\epsilon \propto \Phi$. As this change is small and the calculated results of hydrodynamic quantities are insensitive to Y_e, we set $Y_e = 0.5$ for numerical simplicity.

One of the most important hydrodynamic quantities that characterize the expansion dynamics of the neutrino-driven wind is the dynamic timescale $\tau_{\rm dyn}$, which is the duration of the α-process. When the temperature falls below 10^{10} K, NSE favors a composition of alpha particles and neutrons. As the temperature drops further to below about 5×10^9 K ($T \approx 0.5$ MeV), the system falls out of NSE and the α-process starts accumulating some amount of seed elements until the charged-particle reactions freeze out at $T \approx 0.5/e$ MeV ≈ 0.2 MeV. Introducing a variable for the time the wind takes to move from the distance r_i to the outer distance r_f,

$$\tau = \int_{r_i}^{r_f} \frac{dr}{u}, \quad (22)$$

and setting $r_i = r(T = 0.5$ MeV) and $r_f = r(T = 0.5/e$ MeV), we can define the dynamic timescale $\tau_{\rm dyn}$ by

$$\tau_{\rm dyn} \equiv \int_{T=0.5\ {\rm MeV}}^{T=0.5/e\ {\rm MeV}} \frac{dr}{u}. \quad (23)$$

The second important hydrodynamic quantity, which strongly affects r-process nucleosynthesis that occurs at later times when the temperature cools below 0.2 MeV, is the entropy per baryon, defined by

$$S = \int_R^r \frac{m_N \dot{q}}{uT}\, dr, \quad (24)$$

where $\dot{q}$ is the total net heating rate (eq. [16]). As $S \propto T^3/\rho_b$ with the assumption of radiation dominance, high entropy and high temperature characterize a system with many photons and a low baryon number density. Since high entropy also favors a large fraction of free nucleons in the limit of NSE, it is expected to be an ideal condition for making a high neutron-to-seed abundance ratio. Therefore, the high entropy at the beginning of the α-process is presumed to be desirable for the r-process to be successful.

3. NUMERICAL RESULTS

3.1. *Effects of Relativistic Gravity to Entropy*

The purpose of this section is to discuss both similarities and differences between the relativistic and Newtonian treatments of the neutrino-driven wind. In Figure 3, we show typical numerical results for the radial velocity u, temperature T, and baryon mass density ρ_b of the wind for a neutron star of mass $M = 1.4\ M_\odot$, radius $R = 10$ km, and neutrino luminosity $L_\nu = 10^{51}$ ergs s^{-1}. The radial dependence of these quantities is displayed by solid and dashed curves for the Schwarzschild and Newtonian cases, respectively, in this figure. Using these results and equation (24), we can calculate S in each ejecta. Figure 4 shows the calculated profile of the entropy S for the two cases. Although both entropies describe a rapid increase just above the surface of the neutron star, at 10 km $\le r \le$ 15 km, the asymptotic value in the general relativistic wind is nearly 40% larger than that in Newtonian wind.

The similar behavior of the rapid increases in both winds is due to efficient neutrino heating near the surface of the neutron star. We show the radial dependence of the neutrino heating and cooling rates in Figures 5*a*–5*c*. Figure 5*a* shows the total net heating rate defined by equation (16), and Figures 5*b* and 5*c* display the decompositions into contributions from each heating (*solid curves*) or cooling (*dashed curves*) rate in the Schwarzschild and Newtonian cases, respectively. The common characteristic in both cases is that the net heating rate $\dot{q}$ has a peak around $r \approx 12$ km, which causes a rapid increase in S near the surface of the neutron star for the following reason. The integrand of the entropy S in equation (24) consists of the heating rate and the inverse of the fluid velocity times the temperature. The

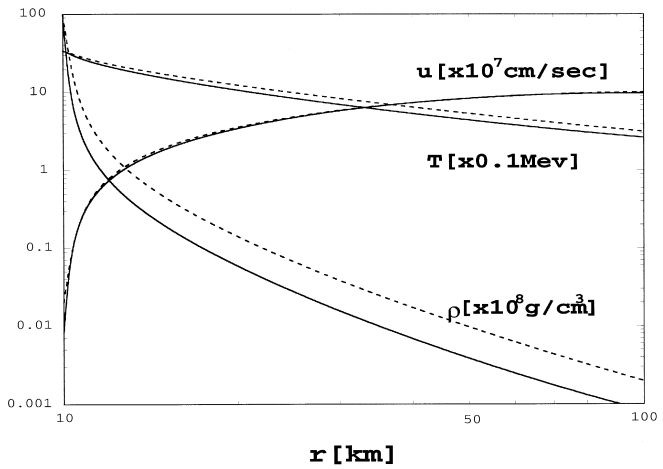

FIG. 3.—Outflow velocity $u(r)$ in units of 10^7 cm s^{-1}, temperature $T(r)$ in units of 0.1 MeV, and baryon mass density $\rho_b(r)$ in unit of 10^8 g cm^{-3} as functions of the distance r from the center of a neutron star with proto–neutron star mass $M = 1.4\ M_\odot$, radius $R = 10$ km, neutrino luminosity $L_\nu = 10^{51}$ ergs s^{-1}, and initial density 10^{10} g cm^{-3}. Solid and dashed lines display the results in the Schwarzschild and Newtonian geometries, respectively. We choose the mass outflow rate $\dot{M} = 5.0855 \times 10^{-6}\ M_\odot$ s^{-1} for the Schwarzschild case and $\dot{M} = 1.2690 \times 10^{-5}\ M_\odot$ for the Newtonian case. See the text for details of the outer boundary condition on $\dot{M}$.

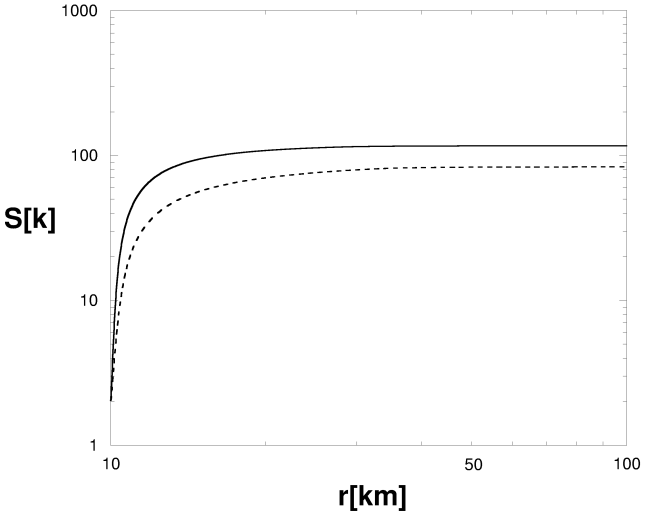

FIG. 4.—Entropy per baryon $S(r)$ as a function of the distance r from the center of the neutron star. Solid and dashed lines are as in Fig. 1 for the same set of input parameters.

fluid velocity increases more rapidly than the slower decrease in the temperature, as shown in Figure 3, after the wind lifts off the surface of the neutron star.

Let us carefully discuss the reason that the general relativistic wind results in a 40% larger entropy than the Newtonian wind in the asymptotic region. This fact has been suggested previously by Qian & Woosley (1996) and Cardall & Fuller (1997). Unfortunately, however, they did not specifically and quantitatively identify which of the several possible sources they discuss was the reason for this difference.

We first consider the redshift effect and the bending effect of the neutrino trajectory. The redshift effect plays a role in decreasing the mean neutrino energy ϵ_ν ejected from the neutrinosphere, and in practice ϵ_ν is proportional to the redshift factor $\Phi(r)$, which is defined by equation (10). Since neutrino luminosity is proportional to Φ^4 and the heating rate $\dot{q}_1$, $\dot{q}_3$, and $\dot{q}_5$ depend on these quantities in different manners, each heating rate has different Φ dependence as $\dot{q}_1 \propto L_\nu \epsilon_\nu^2 \propto \Phi^6$, $\dot{q}_3 \propto L_\nu \epsilon_\nu \propto \Phi^5$, and $\dot{q}_5 \propto L_\nu^2 \epsilon_\nu \propto \Phi^9$, as shown in equations (8), (11), and (12). Cooling rates $\dot{q}_2$ and $\dot{q}_4$ do not depend on $\Phi(r)$. The bending effect of the neutrino trajectory is included in the geometrical factors $g_1(r)$ and $g_2(r)$ in these equations. Although numerical calculations were carried out by including all five heating and cooling processes, as $\dot{q}_1$, $\dot{q}_2$, and $\dot{q}_3$ predominate the total net heating rate $\dot{q}$, for simplicity we limit ourselves to only these three processes in the following discussions.

In Newtonian analysis, the redshift factor $\Phi(r)$ is unity and the geometrical factor is given by

$$g_{1N}(r) = \sqrt{1 - \left(\frac{R_\nu}{r}\right)^2} .$$

This geometrical factor $g_1(r)$ and the redshift factor appear in the form of $[1 - g_1(r)]\Phi(r)^m$ in the heating rate $\dot{q}_1(m = 5)$ and $\dot{q}_3(m = 6)$. As for the first factor $[1 - g_1(r)]$, the following inequality relation holds between the Schwarzschild and Newtonian cases, for $R_\nu \leq r$;

$$[1 - g_1(r)] > [1 - g_{1N}(r)] .$$

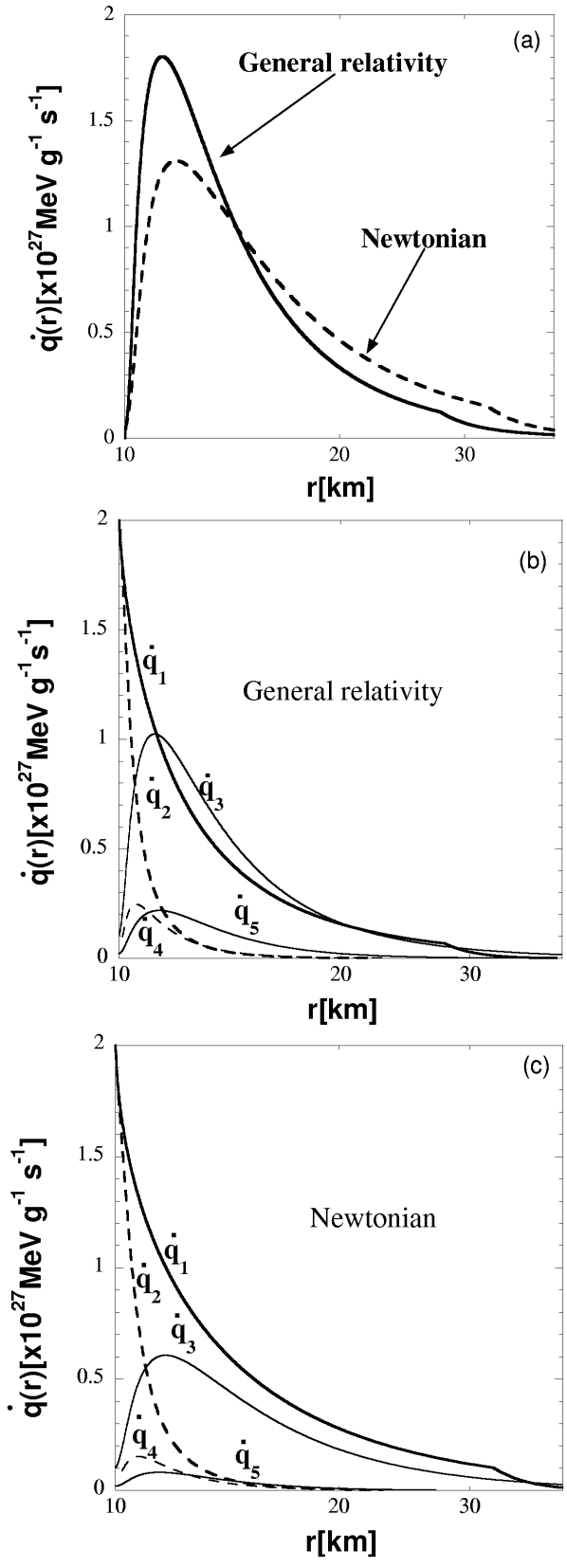

FIG. 5.—Specific neutrino heating rate $\dot{q}(r)$ as a function of distance r from the center of the neutron star for the same set of input parameters as in Fig. 1. (*a*) Total net heating rate $\dot{q}$. The solid and dashed lines are for the Schwarzschild (denoted by general relativity) and Newtonian cases, respectively. (*b*) Decomposition of the net heating rate into five different contributions from the heating processes $\dot{q}_1$, $\dot{q}_3$, and $\dot{q}_5$ (*solid lines*) and the cooling process $\dot{q}_2$ and $\dot{q}_4$ (*dashed lines*) for the Schwarzschild case. See the text for details of $\dot{q}_i$. (*c*) Same as in (*b*) but for the Newtonian case.

However, $\Phi(r)$ is a monotonously decreasing function of r, the combined factor $[1 - g_1(r)]\Phi(r)^m/[1 - g_{1N}(r)]$ increases from unity and has a local maximum around $r \sim R_\nu + 0.2$ km. Its departure from unity is at most 3%. Beyond this radius the function starts to decrease rapidly because of the redshift effect $\Phi(r)^m$, and it becomes as low as ~ 0.6 at $r \sim 30$ km. In this region, the net heating rate in the relativistic wind is smaller than that in the Newtonian wind if the temperature and density are the same. However, the difference in this region does not influence the dynamics of the wind very much. It is determined only when almost in the inner region, $R_\nu \leq r \lesssim 15$ km, where one finds efficient neutrino heating and little difference between $[1 - g_1(r)]\Phi^m(r)$ and $[1 - g_{1N}(r)]$.

By performing the general relativistic calculation and neglecting these two relativistic effects, i.e., the redshift effect and the bending effect of the neutrino trajectory, we find that it produces only a small change in entropy, $\Delta S \sim 3$. Thus it does not seem to be the major source of the increase in the entropy.

Let us consider another source of general relativistic effects that are included in the solution of the set of basic equations (1), (2), and (3). Since the entropy depends on three hydrodynamic quantities $\dot{q}(r)$, $u(r)$, and $T(r)$ (see eq. [24]), we should discuss each quantity. The neutrino-heating rate, $\dot{q}(r)$, depends on the temperature $T(r)$ and the density $\rho_b(r)$ in addition to the redshift factor and the geometrical factor of the bending neutrino trajectory. Therefore, we study first the detailed behavior of $T(r)$, $u(r)$, and $\rho_b(r)$, and then try to find out why the general relativistic effects increase the entropy. We assume that the pressure and internal energy per baryon are approximately described by the radiation and relativistic electrons and positrons in order to make clear the following discussions. This is a good approximation for the neutrino-driven wind. The equations of state are given by

$$P \approx \frac{11\pi^2}{180} T^4 \tag{25}$$

and

$$\epsilon \approx \frac{11\pi^2}{60} \frac{T^4}{\rho_b} . \tag{26}$$

By using another approximation,

$$u^2 \ll \frac{4P}{3\rho_b} , \tag{27}$$

which is satisfied in the region of interest, we find

$$\frac{1}{T}\frac{dT}{dr} \approx \frac{1}{1 + u^2 - (2M/r)} \frac{\rho_b + P}{4P} \times \left(-\frac{M}{r^2} + \frac{2u^2}{r} - \frac{45}{11\pi^2} \frac{u\rho_b}{T^4} \dot{q} \right) \tag{28}$$

in Schwarzschild case. The basic equations of the spherically symmetric, steady state wind in the Newtonian case are given by

$$\dot{M} = 4\pi r^2 \rho_b v , \tag{29}$$

$$v \frac{dv}{dr} = -\frac{1}{\rho_b}\frac{dP}{dr} - \frac{M}{r^2} , \tag{30}$$

and

$$\dot{q} = v\left(\frac{d\epsilon}{dr} - \frac{P}{\rho_b^2}\frac{d\rho_b}{dr} \right) , \tag{31}$$

where v is the fluid velocity. The equations of state are given by equations (4) and (5), the same as in Schwarzschild case. Repeating the same mathematical technique in equations (29), (30), and (31) instead of equations (1), (2), and (3) and taking the same approximations as in equations (25), (26), and (27), we find the equation corresponding to equation (28), in the Newtonian case, to be

$$\frac{1}{T}\frac{dT}{dr} \approx \frac{\rho_b}{4P} \left(-\frac{M}{r^2} + \frac{2v^2}{r} - \frac{45}{11\pi^2} \frac{v\rho_b}{T^4} \dot{q} \right) . \tag{32}$$

Note that the logarithmic derivative of the temperature, $d \ln T/dr = T^{-1} dT/dr$, always has a negative value and that the temperature is a monotonously decreasing function of r. There are two differences between equations (28) and (32). The first prefactor $1/(1 + u^2 - 2M/r)$ in the right-hand side of equation (28) is larger than unity. This causes a more rapid decrease of $T(r)$ in the relativistic case than in the Newtonian case at small radii, within $r \sim 20$ km, as shown in Figure 3, where our approximations are satisfied. The second prefactor $(\rho_b + P)/4P$ in the right-hand side of equation (28) is larger than the prefactor $\rho_b/4P$ in the right-hand side of equation (32), i.e., $(\rho_b + P)/4P > \rho_b/4P$, which also makes the difference caused by the first prefactor even larger.

Applying the similar mathematical transformations to the velocity, we obtain the following approximations:

$$\frac{1}{u}\frac{du}{dr} \approx \frac{3}{1 + u^2 - (2M/r)} \frac{(\rho_b + 4P)}{4P} \frac{M}{r^2} - \frac{2}{3r} + \frac{\rho_b}{4uP} \dot{q} \tag{33}$$

in the Schwarzschild case, and

$$\frac{1}{v}\frac{dv}{dr} \approx \frac{3\rho_b}{4P}\frac{M}{r^2} - \frac{2}{3r} + \frac{\rho_b}{4vP} \dot{q} \tag{34}$$

in the Newtonian case. In these two equations, the first leading term in the right-hand side makes the major contribution. Since exactly the same prefactors $1/(1 + u^2 - 2M/r)$ and $(\rho_b + 4P)/4P$ appear in the Schwarzschild case, the same logic as in the logarithmic derivative of the temperature is applied to the velocity. Note, however, that slightly different initial velocities at the surface of the neutron star make this difference unclear in Figure 3. The relativistic Schwarzschild wind starts from $u(10 \text{ km}) \approx 8.1 \times 10^4$ cm s^{-1}, while the Newtonian wind starts from $v(10 \text{ km}) \approx 2.0 \times 10^5$ cm s^{-1}. Both winds reach almost the same velocity at around $r \sim 20$ km or beyond.

The baryon number conservation leads to the logarithmic derivative of the baryon density

$$\frac{1}{\rho_b}\frac{d\rho_b}{dr} = -\frac{1}{u}\frac{du}{dr} - \frac{2}{r} , \tag{35}$$

where u is the radial component of the four-velocity in the Schwarzschild case. The fluid velocity v should be read for u in Newtonian case. Inserting equation (33) or equation (34) into the first term on the right-hand side of this equation, we can predict the behavior of ρ_b as a function of r in both the Schwarzschild and Newtonian cases, as shown in Figure 3.

Incorporating these findings concerning $T(r)$, and $u(r)$ into the definition of entropy, equation (24), we can now

discuss why the relativistic Schwarzschild wind makes more entropy than the Newtonian wind. We have already noted in the second paragraph of this section that the fluid velocity increases more rapidly in the Schwarzschild case. Since the integrand of the entropy S is inversely proportional to the fluid velocity times the temperature, this fact increases the difference due to $\dot{q}$ at smaller radii (see Fig. 4*a*). In addition, as we found, the temperature in the Schwarzschild geometry is smaller than that in the Newtonian geometry. For these reasons, the entropy in the relativistic Schwarzschild wind becomes larger than the entropy in the Newtonian wind.

Let us confirm the present results quantitatively in a different manner. The entropy per baryon for relativistic particles with zero chemical potential is given by

$$S = \frac{11\pi^2}{45} \frac{T^3}{\rho_b/m_N} . \tag{36}$$

Here, we take a common temperature $T = 0.5$ MeV for both the Schwarzschild and Newtonian cases. This is the typical temperature at the beginning of the α-process, and both electrons and positrons are still relativistic at this temperature. We read off the radii at which the temperature reaches 0.5 MeV in Figure 3. They are 43 and 55 km in the Schwarzschild and Newtonian cases, respectively. We can again read off the baryon mass densities at these radii in this figure, and we find that $\rho_b = 5.5 \times 10^5$ g cm^{-3} at $r = 43$ km in the relativistic Schwarzschild wind and $\rho_b = 7.8 \times 10^5$ g cm^{-3} at $r = 55$ km in the Newtonian wind. Taking the inverse ratio of these ρ_b values with the approximate relation (36), we find that the entropy in the Schwarzschild case is 40% larger than that in the Newtonian case. This is quantitatively in good agreement with the result of the numerical calculation shown in Figure 4.

Let us briefly remark on the dynamic timescale $\tau_{\rm dyn}$. Although higher entropy is favorable for making enough neutrons in the neutrino-driven wind, a shorter dynamic timescale also favors the r-process. This is because the neutron-to-seed abundance ratio, which is one of the critical parameters for the r-process to be successful, becomes larger in the wind with shorter $\tau_{\rm dyn}$, as we discuss in the next section. It is therefore worthwhile to discuss the general relativistic effect on $\tau_{\rm dyn}$ here. The argument is evident from equations (28) and (32) and Figure 3. Since the dynamic timescale $\tau_{\rm dyn}$ is defined as the duration of the α-process, in which the temperature of the wind cools from $T = 0.5$ MeV to $T = 0.5/e \approx 0.2$ MeV, faster cooling is likely to result in shorter $\tau_{\rm dyn}$. Let us demonstrate this numerically. For the reasons discussed below equations (28) and (32), the relativistic fluid describes a more rapid decrease in temperature than the Newtonian fluid as a function of distance r. In fact, the distances corresponding to $T = 0.5$–0.2 MeV are $r = 43 - 192$ km in the Schwarzschild case and $r = 55$–250 km in the Newtonian case. Figure 3 tells us that both fluids have almost the same velocities at these distances, which gives a shorter $\tau_{\rm dyn}$ for the Schwarzschild case than for the Newtonian case. The calculated dynamic timescales are $\tau_{\rm dyn} = 0.164$ s for the former and $\tau_{\rm dyn} = 0.213$ s for the latter.

Before closing this subsection, let us briefly discuss how the system makes a complicated response to the change in $T(r)$, $u(r)$, and $\rho_b(r)$. When the temperature decreases rapidly at 10 km $\le r \lesssim 20$ km, the major cooling process of e^+e^- capture by free nucleons, $\dot{q}_2$, is suppressed because this cooling rate has a rather strong temperature dependence, $\dot{q}_2 \propto T^6$. In Schwarzschild geometry this suppression partially offsets the decrease in $\dot{q}_1$ due to the neutrino redshift effect, though it is independent of temperature of the wind. Another heating source, $\dot{q}_3$, due to neutrino-electron scattering, also plays a role in the change of entropy. Since $\dot{q}_3$ depends on the baryon density as well as temperature, $\dot{q}_3 \propto T^4/\rho_b$, if the system has a correlated response to decrease ρ_b strongly with decreasing temperature, then this might eventually work for the partial increase in entropy. However, in reality, the actual response arises from a more complicated mechanism because $\dot{q}_i$'s should depend on the solution of dynamic equations (1), (2), and (3) self-consistently with the adopted proper boundary conditions and input parameters through the relations $\dot{q}_1 \propto L_\nu \epsilon_\nu^2$, $\dot{q}_2 \propto T^6$, $\dot{q}_3 \propto T^4/\rho_b L_\nu \epsilon_\nu$, $\dot{q}_4 \propto T^9/\rho_b$, and $\dot{q}_5 \propto \rho_b^{-1} L_\nu^2 \epsilon_\nu$. The neutrino-driven wind is a highly nonlinear system.

3.2. *Parameter Dependence*

Most of the previous studies of the neutrino-driven wind have concentrated on SN 1987A, and the parameter set in the theoretical calculations was almost exclusive. We here expand our parameter region of the neutron star mass M, radius R, and neutrino luminosity L_ν and investigate widely the dependence of the key quantities $\tau_{\rm dyn}$ and S on these three parameters. Since the neutron star mass M and radius R are mostly contained through the form M/R in the basic equations of the system, we look only at the dependence on M and L_ν.

Figures 6*a* and 6*b* show the calculated $\tau_{\rm dyn}$ and S at the beginning of the α-process at $T = 0.5$ MeV for various neutron star masses $1.2\ M_\odot \le M \le 2.0\ M_\odot$ for the Schwarzschild (*closed circles*, connected by the *thick solid line*) and Newtonian (*open triangles*, connected by the *thin solid line*) cases. In Figure 6*a*, we also plot the Newtonian case from Qian & Woosley (1996; *dashed lines*), who adopted

$$\tau_{\rm dyn}({\rm QW}) = \left| \frac{r}{v} \right|_{0.5\ {\rm MeV}} , \tag{37}$$

in the upper limit of the radiation dominance and the lower limit of the dominance of nonrelativistic nucleons. In either limit, this $\tau_{\rm dyn}$(QW) is an increasing function of the neutron star mass, and this feature is in reasonable agreement with our exact solution, equation (23). However, the absolute value of equation (37) is about one-half that of the exact solution in the Newtonian case.

A remarkable difference between the Schwarzschild and Newtonian cases is the opposite response of $\tau_{\rm dyn}$ to the neutron star mass (Fig. 6*a*). General relativistic effects make the dynamic timescale even smaller with increasing neutron star mass. We have already discussed the why $\tau_{\rm dyn}$ in the Schwarzschild case is smaller than in the Newtonian case by comparing equations (28) and (32). We understand that the decrease of $\tau_{\rm dyn}$ is a consequence of the fact that the general relativistic effects, which arise from the two prefactors in the right-hand side of equation (28), are enlarged by the stronger gravitational force M/r^2 with larger M. Similar analysis of the role of the gravitational force is applied to the discussion of entropy and equations (28), (33), and (35). Figure 6*b* shows that the entropy per baryon in the Schwarzschild case leads to a stronger mass dependence than in the Newtonian case.

It is to be noted again that the above features of the mass dependence are equivalent to those obtained by a change in

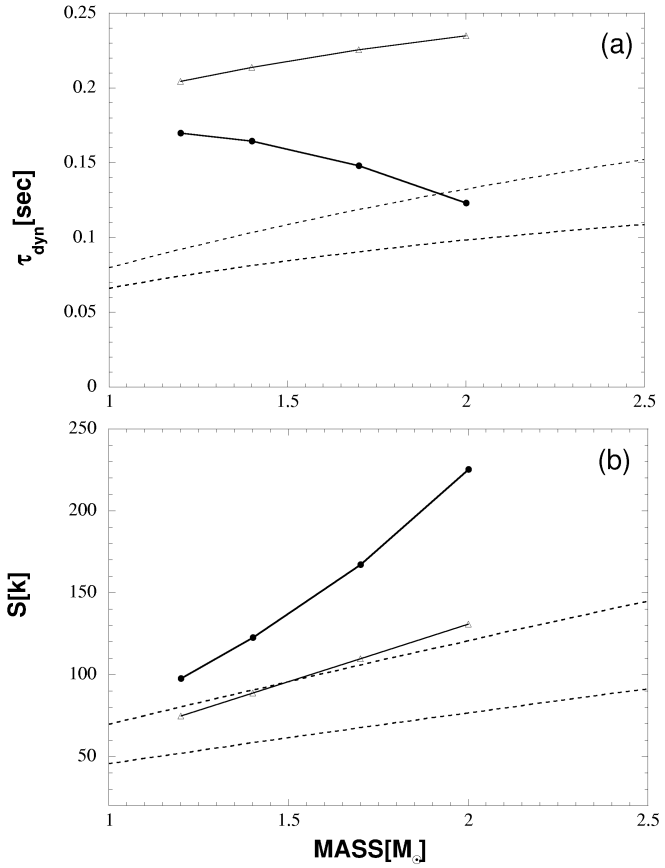

FIG. 6.—Dynamic timescale τ_{dyn} *a* and entropy per baryon S *b* vs. neutron star mass M at 0.5 MeV. Closed circles connected by thick solid lines and open triangles connected thin solid lines are the calculated results for the Schwarzschild and Newtonian cases, respectively, using the same set of input parameters as in Fig. 1. The two dashed lines are from Qian & Woosley (1996) in Newtonian case, which adopted an assumption of radiation dominance or dominance of nonrelativistic nucleon in (*a*) τ_{dyn} and (*b*) S.

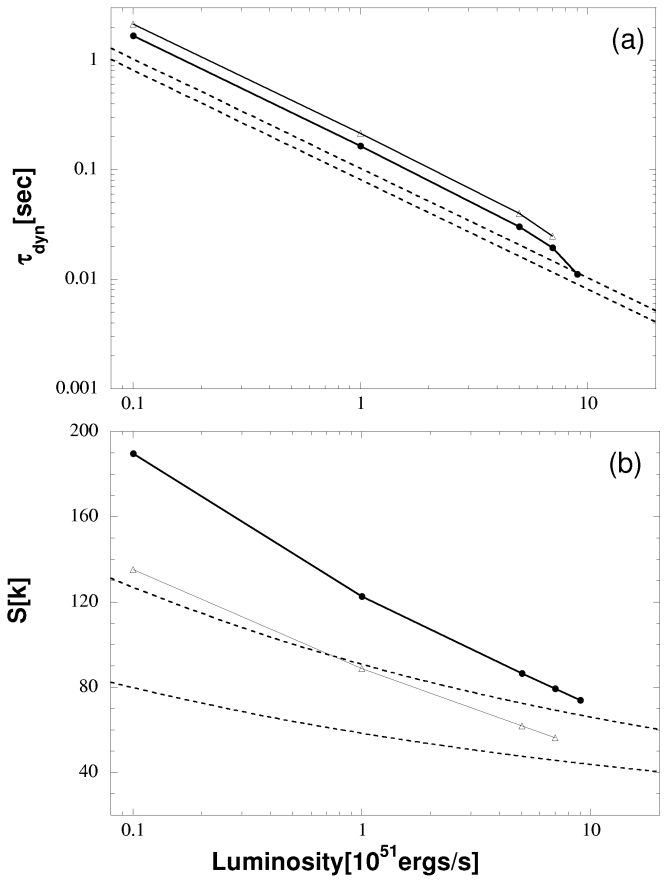

FIG. 7.—Dynamic timescale τ_{dyn} *a* and entropy per baryon S *b* vs. neutrino luminosity L_ν at $T = 0.5$ MeV. Lines are as in Fig. 4. At the larger end, $L_\nu \sim 10^{52}$ ergs s^{-1}, there is no solution to satisfy our imposed boundary condition, $T = 0.1$ MeV at $r = 10{,}000$ km. See text details.

the neutron star radius. Since the radius of the proto–neutron star shrinks with time in the cooling process, it may work to increase the entropy and decrease the dynamic timescale.

Figures 7*a* and 7*b* show the dependence of our calculated τ_{dyn} and S on neutrino luminosity in the range 10^{50} ergs s$^{-1} \leq L_\nu \leq 10^{52}$ ergs s^{-1}. Unlike in the mass dependence, both quantities are decreasing functions of L_ν as long as $L_\nu \leq 10^{52}$ ergs s^{-1}. This tendency, except for the absolute values, is in reasonable agreement with the approximate estimates (Qian & Woosley 1996), shown by broken lines. This is because the larger luminosity makes the mass outflow rate $\dot{M}$ higher through more efficient neutrino heating, which causes a bigger increase in the fluid velocity in addition to a moderate increase in the baryon density. Having these changes in hydrodynamic quantities with the definition of τ_{dyn}, equation (23), and the definition of S, equation (24), we understand that both quantities decrease with increasing neutrino luminosity.

However, if the luminosity becomes larger than 10^{52} ergs s^{-1}, the temperature does not decrease to as low as 0.1 MeV before the distance reaches 10,000 km because of the effect of too strong neutrino heating. The dynamic timescale τ_{dyn} is of order ~ 10 s. In such a very slow expansion of the neutrino-driven wind, the α-process takes place and leads to uninteresting *r*-process nucleosynthesis.

To summarize this section, we find it difficult to obtain very large entropy, ~ 400, for reasonably short dynamic timescales, $\tau_{dyn} \lesssim 0.1$ s, as reported by Woosley et al. (1994), by changing the neutron star mass M and neutrino luminosity L_ν. However, there are still significant differences between our calculated results for τ_{dyn} and S (*thick solid lines* in Figs. 6*a*–7*b*) and those of Qian & Woosley (1996; *dashed lines*) in the mass dependence of the entropy and the opposite behavior in τ_{dyn}. We will see in the subsequent sections that these differences are important to look for in considering conditions for the *r*-process to be successful.

3.3. *Implication in Nucleosynthesis*

Having known the detailed behavior of dynamic timescale τ_{dyn} and entropy per baryon S as a function of neutron star mass M, radius R, and neutrino luminosity L_ν, we are forced to discuss their implications for *r*-process nucleosynthesis. We have already shown the calculated results of τ_{dyn} and S for limited sets of two independent parameters M and L_ν in Figures 6*a*–7*b*. We here expand the parameter space in order to include a number of (M, L_ν) grids in reasonable ranges, $1.2\ M_\odot \leq M \leq 2.0\ M_\odot$ and 10^{50} ergs s$^{-1} \leq L_\nu \leq 10^{52}$ ergs s^{-1}.

Figure 8 displays the calculated results in the τ_{dyn}-S plane. Shown also are two zones for which the second abundance peak around $A = 130$ and the third abundance peak around $A = 195$ might be formed by *r*-process as suggested by Hoffman, Woosley, & Qian 1997). Their condition for the element with mass number A to be produced in an

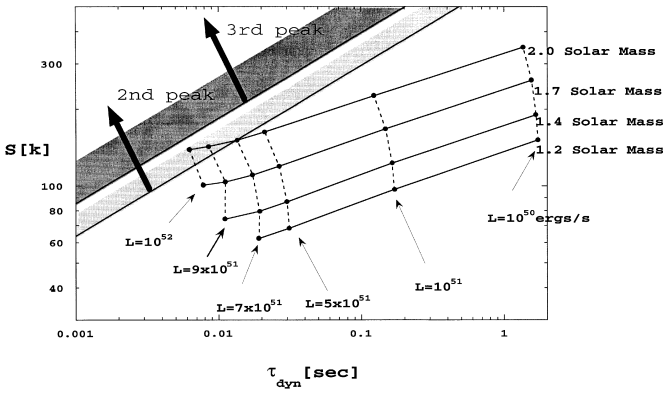

FIG. 8.—Relation between entropy per baryon S and dynamic timescale $\tau_{\rm dyn}$ for various combinations of neutron star mass $1.2\ M_\odot \le M \le 2.0\ M_\odot$ and neutrino luminosity $10^{50} \le L_\nu \le 10^{52}$ ergs s^{-1}. Solid and dashed lines connect the same masses and luminosities. At the largest end, $L_\nu \sim 10^{52}$ ergs s^{-1} for each M, there is no solution to satisfy our imposed boundary condition, $T = 0.1$ MeV at $r = 10{,}000$ km. Two zones (*shaded*) satisfy the approximate conditions for $Y_e = 0.4$ on which the successful r-process occurs (Hoffman et al. 1997) to make the second abundance peak around $A = 130$ (*lower shaded area*) and the third abundance peak around $A = 195$ (*upper shaded area*). See text for details.

explosive r-process nucleosynthesis, for $Y_e > \langle Z\rangle/\langle A\rangle$, is given by

$$S \approx Y_{e,i}\left\{\frac{8\times 10^7(\langle A\rangle - 2\langle Z\rangle)}{\ln[(1-2\langle Z\rangle/A)/(1-\langle A\rangle/A)]}\left(\frac{\tau_{\rm dyn}}{\rm sec}\right)\right\}^{1/3}, \tag{38}$$

where $\langle A\rangle$ is mean mass number and $\langle Z\rangle$ is mean proton number of the seed nuclei at the end of the α-process. Following numerical survey of seed abundance of Hoffman et al. (1997), we choose $\langle A\rangle = 90$ and $\langle Z\rangle = 34$ in Figure 8. From this figure, we find that a dynamic timescale as short as $\tau_{\rm dyn} \approx 6$ ms with $M = 2.0\ M_\odot$ and $L_\nu = 10^{52}$ ergs s^{-1} is the best case among those studied in the present paper for producing the r-process elements, although the entropy S is rather small, 140.

Let us remark briefly on this useful equation. Equation (38) tells us that the r-process element with mass number A is efficiently produced from seed elements with $\langle A\rangle$ and $\langle Z\rangle$ with given physical conditions $\tau_{\rm dyn}$, S, and Y_e at the onset of r-process nucleosynthesis at $T_9 \approx 2.5$. In order to derive equation (38), Hoffman et al. (1997) assumed that the $\alpha + \alpha + n \rightarrow {}^9{\rm Be} + \gamma$ reaction is in equilibrium, because of its low Q value, during the α-process at $T \approx 0.5$–0.2 MeV and that the ${}^9{\rm Be} + \alpha \rightarrow {}^{12}{\rm C} + \gamma$ reaction triggers the burning of alpha particles to accumulate seed elements. NSE is maintained if the nuclear interaction timescale for $\alpha + \alpha + n \rightarrow {}^9{\rm Be} + \gamma$ is much shorter than the expansion timescale. We found in the present calculation that this is not always the case in neutrino-driven winds with short dynamic timescales for $L_\nu \approx 5\times 10^{51}$–$10^{52}$ ergs s^{-1}, as will be discussed more quantitatively in the next section. Keeping this in mind, we think that equation (38) is still a useful formula for searching for suitable physical conditions for the r-process without performing numerical nucleosynthesis calculations.

One might wonder if the dynamic timescale $\tau_{\rm dyn} \sim 6$ ms is too short to allow the wind to be heated by neutrinos. A careful comparison of the proper expansion time with the specific collision time for neutrino heating is needed in order to answer this question. Note that $\tau_{\rm dyn}$ was defined as the α-process duration over which the temperature of the expanding wind decreases from $T = 0.5$ to $0.5/e \approx 0.2$ MeV, which corresponds to the outer atmosphere of a neutron star. These radii are $r(T = 0.5\ {\rm MeV}) = 52$ km and $r(T = 0.5/e\ {\rm MeV}) = 101$ km for the wind with $(L_\nu, M) = (10^{52}\ {\rm ergs\ s^{-1}}, 2.0\ M_\odot)$, and $r(T = 0.5\ {\rm MeV}) = 43$ km and $r(T = 0.5/e\ {\rm MeV}) = 192$ km for the wind with $(L_\nu, M) = (10^{51}\ {\rm ergs\ s^{-1}}, 1.4\ M_\odot)$. We found in Figures 5*a*–5*c* that the neutrinos transfer their kinetic energy to the wind most effectively just above the neutron star surface, at 10 km $\le r <$ 20 km. Therefore, as for the heating problem, one should refer the duration of time for the wind to reach the radius where temperature is $T \approx 0.5$ MeV rather than $\tau_{\rm dyn}$. We can estimate this expansion time $\tau_{\rm heat}$ by setting $r_i = R = 10$ km and $r_f = r(T = 0.5\ {\rm MeV})$ in equation (22): $\tau_{\rm heat} = 0.017$ s and 0.28 s for winds with $(L_\nu, M) = (10^{52}$ ergs s^{-1}, 2.0 $M_\odot)$ and $(10^{51}$ ergs s^{-1}, 1.4 $M_\odot)$, respectively. We note, for completeness, that $r(T = 0.5\ {\rm MeV}) = 52$ km or 43 km for each case.

These proper expansion timescales, $\tau_{\rm heat}$, are to be compared with the specific collision time τ_ν for the neutrino-nucleus interactions in order to discuss the efficiency of the neutrino heating. The collision time τ_ν is expressed (Qian et al. 1997) as

$$\tau_\nu \approx 0.201 \times L_{\nu,51}^{-1}\left(\frac{\epsilon_\nu}{\rm MeV}\right)\left(\frac{r}{100\ {\rm km}}\right)^2\left(\frac{\langle\sigma_\nu\rangle}{10^{-41}\ {\rm cm^2}}\right)^{-1}\ {\rm s}\,, \tag{39}$$

where $L_{\nu,51}$ and ϵ_ν have already been defined in § 2.1, and $\langle\sigma_\nu\rangle$ is the averaged cross section over the neutrino energy spectrum. As discussed above, neutrino heating occurs most effectively at $r \approx 12$ km (see also Fig. 5*a*), and we set this value in equation (39). Since two neutrino processes (6) and (7) make the biggest contributions to heating the wind and $\epsilon_{\nu_e} = 12$ MeV and $\epsilon_{\bar\nu_e} = 22$ MeV, we set $\epsilon_\nu = (\epsilon_{\nu_e} + \epsilon_{\bar\nu_e})/2 \approx 15$ MeV. We take $\langle\sigma_\nu\rangle = 10^{-41}$ cm^2. Incorporating these values into equation (39), we can obtain the value of τ_ν. Let us compare the specific collision time, τ_ν, and the proper expansion time, $\tau_{\rm heat}$:

$$\tau_\nu = 0.0043\ {\rm s} < \tau_{\rm heat} = 0.017\ {\rm s}\,,$$
$$\text{for } (L_\nu, M) = (10^{52}\ {\rm ergs\ s^{-1}}, 2.0\ M_\odot)\,, \tag{40a}$$
$$\tau_\nu = 0.043\ {\rm s} < \tau_{\rm heat} = 0.28\ {\rm s}\,,$$
$$\text{for } (L_\nu, M) = (10^{51}\ {\rm ergs\ s^{-1}}, 1.4\ M_\odot)\,. \tag{40b}$$

We can conclude that there is enough time for the expanding wind to be heated by neutrinos even with a short dynamic timescale for the α-process, $\tau_{\rm dyn} \sim 6$ ms, which corresponds to the case (40a).

Before closing this section, let us briefly discuss the effect of electron fraction Y_e on the hydrodynamic condition of the neutrino-driven wind. Although we took $Y_e = 0.5$ for simplicity in our numerical calculations, we should quantitatively examine the sensitivity of the calculated result to Y_e. Since we are interested in short dynamic timescales, let us investigate the case with $(L_\nu, M) = (10^{52}$ ergs s^{-1}, 2.0 $M_\odot)$, which results in $S = 138.5$ and $\tau_{\rm dyn} = 0.00618$ s for $Y_e = 0.5$. When we adopt $Y_e = 0.4$, these quantities change slightly to $S = 141.5$ and $\tau_{\rm dyn} = 0.00652$ s. These are very small

changes, less than 5%, and the situation is similar for the other sets of (L_ν, M).

To summarize this section, we found that there is a parameter region in Figure 8 that leads to desirable physical conditions for r-process nucleosynthesis. A sophisticated supernova simulation (Woosley et al. 1994) indicates that the neutrino luminosity from the proto–neutron star decreases slowly from about 5×10^{52} to 10^{51} ergs s^{-1} as the time after the core bounce increases. Therefore, our favorable neutrino luminosity $L_\nu = 10^{52}$ ergs s^{-1} is possible in reality during the relatively earlier epoch of the supernova explosion at around 0.5 s to a few seconds after the core bounce.

4. r-PROCESS NUCLEOSYNTHESIS CALCULATION

Our discussion of r-process nucleosynthesis in the last section was based on Hoffman's criterion, equation (38), which should be used with caution because of several assumptions and approximations adopted in its derivation. The purpose of this section is to confirm quantitatively that the r-process occurs in neutrino-driven winds with short dynamic timescales, which we found in the present study.

Given the flow trajectory characterized by $u(t)$, $\rho_b(t)$, and $T(t)$, as discussed in the last section, our nucleosynthesis calculation starts from the time when the temperature is $T_9 = 9$. Since this temperature is high enough for the system to be in NSE, its initial nuclear composition consists of free neutrons and protons. We set $Y_e = 0.4$ in order to compare our calculation with Hoffman's criterion, shown in Figure 8. In our nucleosynthesis calculation we used a fully implicit single network code for the α- and r-processes that includes over 3000 isotopes. We take the thermonuclear reaction rates for all relevant nuclear processes and their inverse reactions as well as weak interactions from F. K. Thielemann (1995, private communication) for the isotopes with $Z \leq 46$ and from Cowan, Thielemann, & Truran (1991) for the isotopes with $Z > 46$. Previous r-process calculations had the complexity that the seed abundance distribution at $T_9 = 2.5$ was not fully shown in literature (Woosley et al. 1994; Woosley & Hoffman 1992; Hoffman et al. 1997), making the interpretation of the whole nucleosynthesis process less transparent. This inconvenience happened because it was numerically too demanding to run both the α- and r-processes in a single network code for the huge number of reaction couplings among $\sim$3000 isotopes. For this reason, one had to calculate the α-process first, using a smaller network for light-to-intermediate mass elements, in order to provide the seed abundance distribution at $T_9 = 2.5 (T \approx 0.2$ MeV). Adopting such a seed abundance distribution and following the evolution of material in the wind after $T \approx 0.2$ MeV, which is the onset temperature of the r-process, the r-process nucleosynthesis calculation was extensively carried out by using another network code independent of the α-process. Our nucleosynthesis calculation is completely free from this complexity because we exploited a single network code that is applied to a sequence of the entire NSE α- and r-processes.

The calculated mass abundance distribution is shown in Figures 9 and 10 for the neutrino-driven wind with (L_ν, M) = (10^{52} ergs s^{-1}, 2.0 $M_\odot$), which makes most favorable conditions for r-process nucleosynthesis with the shortest $\tau_{\rm dyn} = 0.0062$ s among those studied in the present paper (see Fig. 8). Figure 9 displays the snapshot at the time when the temperature cooled to $T_9 = 2.5 (\approx 0.2$ MeV) at the end of the α-process. This shows seed abundance distribution at the onset of the r-process, too. Our calculated quantities at this temperature are the baryon mass density $\rho_b = 3.73 \times 10^4$ g cm^{-3}, neutron mass fraction $X_n = 0.159$, mass fraction of alpha-particles $X_\alpha = 0.693$, average mass number of seed nuclei $\langle A \rangle = 94$, and neutron-to-seed abundance ratio $n/s = 99.8$ for the set of hydrodynamic quantities $\tau_{\rm dyn} = 0.0062$ s, $S \approx 139$, and $Y_e = 0.4$. These values should be compared with those adopted in Woosley's calculation of his trajectory 40, i.e., $\rho_b = 1.107 \times 10^4$ g cm^{-3}, $X_n = 0.176$, $X_\alpha = 0.606$, $\langle A \rangle = 95$, $n/s = 77$, $\tau_{\rm dyn} \approx 0.305$ s, $S \approx 400$, and $Y_e = 0.3835$, as in Table 3 in Woosley et al. (1994). It is interesting to point out that our seed abundance distribution in Figure 9 is very similar to theirs (Woosley et al. 1994; Woosley & Hoffman 1992), as is clearly shown by their very similar values of $\langle A \rangle \approx 95$, although the other evolutionary parameters and thermodynamic quantities are different. The calculated final r-process abundance is displayed in Figure 10. Our wind model can produce the second ($A \approx 135$) and third ($A \approx 195$) r-process abundance peaks and the rare earth elements between them as well.

It is generally accepted that the r-process elements will be produced if there are plenty of free neutrons and if the neutron-to-seed abundance ratio is high enough to approx-

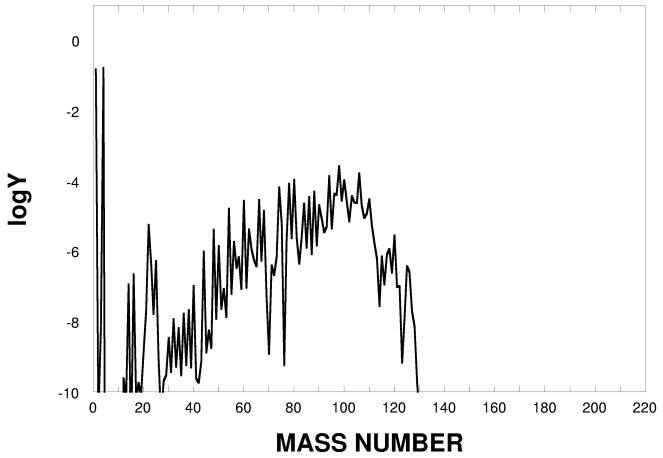

FIG. 9.—Seed abundances at $T_9 = 2.5$ as a function of atomic number A. See text for details.

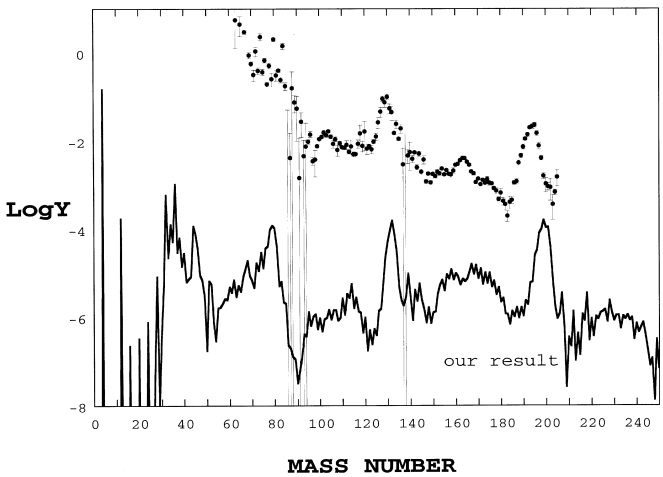

FIG. 10.—Final r-process abundances (*lines*) as a function of atomic mass number A compared with the solar system r-process abundances (*filled circles*) from Käppeler et al. (1989). The solar system r-process abundances are shown in arbitrary units. See text for details.

imately satisfy $A \approx \langle A \rangle + n/s$ (Hoffman et al. 1997) at the beginning of the r-process, where A is the typical mass number of the r-process element. Therefore, the α-process should be the key to understanding why our wind model results in r-process nucleosynthesis similar to the results of Woosley's trajectory 40.

The α burning starts when the temperature cools below $T = 0.5$ MeV. Since the triple-alpha reaction $^4\mathrm{He}(\alpha\alpha, \gamma)^{12}\mathrm{C}$ is too slow at this temperature, an alternative nuclear reaction path to reach $^{12}\mathrm{C}$, $^4\mathrm{He}(\alpha n, \gamma)^9\mathrm{Be}(\alpha, n)^{12}\mathrm{C}$ triggers the explosive α-process to produce the seed elements. In the rapidly expanding flow of a neutrino-driven wind with short τ_{dyn}, it is not a good approximation to assume that the first reaction $^4\mathrm{He}(\alpha n, \gamma)^9\mathrm{Be}$ is in NSE. The rate equation is thus written as

$$\frac{dY_9}{dt} \approx \rho_b\, Y_\alpha^2\, Y_n\, \lambda(\alpha\alpha n \rightarrow {}^9\mathrm{Be}) - \rho_b\, Y_\alpha\, Y_9\, \lambda({}^9\mathrm{Be}\alpha \rightarrow {}^{12}\mathrm{C}) + (\text{their inverses and other reaction rates}), \quad (41)$$

where Y_9, Y_α, Y_n are the number fractions of $^9\mathrm{Be}$, alpha particles, and neutrons, and $\lambda(\alpha\alpha n \rightarrow {}^9\mathrm{Be})$ and $\lambda({}^9\mathrm{Be}\alpha \rightarrow {}^{12}\mathrm{C})$ are the thermonuclear reaction rates for each reaction process, as indicated. Details on λ are reported in Woosley & Hoffman (1992) and Wrean, Brune, & Kavanagh (1994). Let us take the first term of the right-hand side of equation (41), which is the largest of all terms in equation (41). This is allowed in the following discussion of the timescale because the $^4\mathrm{He}(\alpha n, \gamma)^9\mathrm{Be}$ reaction is the slowest among all the charged particle reaction paths in all the α-process reactions. We now define the typical nuclear reaction timescale τ_α of the α-process, regulated by the $^4\mathrm{He}(\alpha n, \gamma)^9\mathrm{Be}$ reaction timescale τ_N, as

$$\tau_\alpha \gtrsim [\rho_b\, Y_\alpha^2\, Y_n\, \lambda(\alpha\alpha n \rightarrow {}^9\mathrm{Be})]^{-1} \equiv \tau_N\,. \quad (42)$$

We show the ratio $\tau_{\mathrm{dyn}}/\tau_N$ as a function of the baryon mass density ρ_b at the beginning of the α-process when $T = 0.5$ MeV for wind models with various values of (L_ν, M) in Figure 11. Note that the critical line $\tau_{\mathrm{dyn}}/\tau_\alpha = 1$ is slightly shifted upward because of $\tau_N \lesssim \tau_\alpha$. This figure, with the help of Figure 8, clearly indicates that the favorable conditions for the r-process nucleosynthesis have inevitably shorter $\tau_{\mathrm{dyn}} \ll \tau_N$ and τ_α. The typical ratio is of order $\tau_{\mathrm{dyn}}/\tau_N \sim 0.1$.

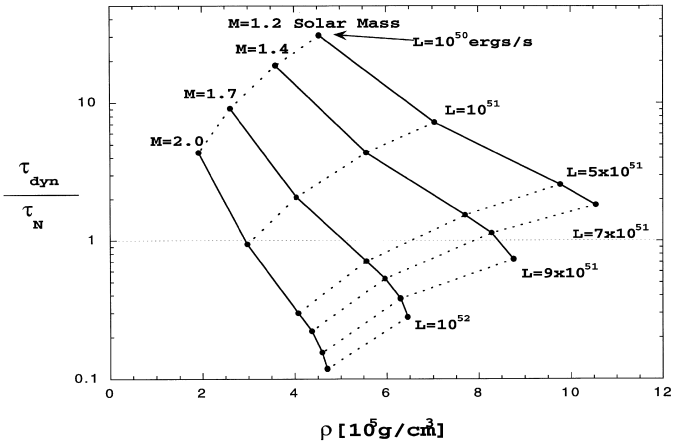

FIG. 11.—Ratio of dynamic timescale τ_{dyn} to the timescale of typical α-process nuclear reaction τ_N, $\tau_{\mathrm{dyn}}/\tau_N$, vs. baryon mass density at $T = 0.5$ MeV, for various combinations of neutron star mass $1.2\ M_\odot \le M \le 2.0\ M_\odot$ and neutrino luminosity $10^{50} \le L_\nu \le 10^{52}$ ergs s^{-1}. Solid and dashed lines connect the same masses and luminosities.

The interpretation of this result is that there is not enough time for the α-process to accumulate a number of seed elements and plenty of free neutrons are left even at the beginning of the r-process. Consequently, the n/s ratio becomes very high ~ 100.

As for the neutron mass fraction, on the other hand, our value $X_n = 0.159$ is smaller than Woosley's model value $X_n = 0.176$ in trajectory 40 because low entropy favors a low neutron fraction. This may be a defect in our low-entropy model. However, the short dynamic timescale saves the situation by regulating the excess of the seed elements as discussed above. These two effects compensate for each other, resulting in an average mass number of seed nuclei $\langle A \rangle \approx 95$ and a neutron-to-seed abundance ratio $n/s \approx 100$, which is ideal for the production of the third ($A \approx 195$) abundance peak of the r-process elements in our model, as displayed in Figure 10.

The r-process elements have recently been detected in several metal-deficient halo stars (Sneden et al. 1996), and the relative abundance pattern for the elements between the second and the third peaks proves to be very similar to that of the solar system r-process abundances. One of the possible and straightforward interpretations of this fact is that they were produced in a narrow window of some limited physical condition in massive supernova explosions, as studied in the present paper. These massive stars have short lives $\sim 10^7$ yr and have ejected nucleosynthesis products into the interstellar medium continuously from the early epoch of Galaxy evolution. It is not meaningless, therefore, to discuss several features of our calculated result in comparison with the solar system r-process abundance distribution (Käppeler, Beer, & Wisshak 1989) in Figure 10. Although Käppeler et al. obtained these abundances as s-process subtractions from the observed meteoritic abundances (Anders & Grevesse 1989) for the mass region $63 \le A \le 209$, the inferred yields and error bars for $A = 206,207,208$, and 209 are subject to a still-uncertain s-process contribution. We did not show these heavy elements $A = 206$–209 in Figure 10.

Our single-wind model reproduces observed abundance peaks around $A \approx 130$ and $A \approx 195$ and the rare earth element region between these two peaks. However, there are several requirements to the wind model in order to better fit the details of the solar system r-process abundances in the mass region $120 \lesssim A$. The first unsatisfactory feature in our model calculation is that the two peaks are shifted upward by ~ 2–4 mass units, although the overall positions and peaks are in good agreement with the solar system data. This is a common problem in all theoretical calculations of r-process nucleosynthesis (Meyer et al. 1992; Woosley et al. 1994). The shift of the peak around $A \approx 195$ is slightly larger than that around $A \approx 130$, which may be attributed to strong neutron exposure, as represented by $n/s \approx 100$ in our model calculation. The second feature is that the rare earth element region shows a broad abundance hill, but its peak position $A \approx 165$ in the data is not explained in our calculation. It was pointed out by Surman et al. (1997) that the abundance structure in this mass region is sensitive to a subtle interplay of nuclear deformation and beta decay just prior to the freeze-out of the r-process. More careful studies of these nuclear effects and the dynamics of r-process nucleosynthesis are desirable. The third failure in the model calculation is the depletion around $A \approx 120$, which is also another serious problem encountered by all previous theo-

retical calculations. This deficiency is thought to be made by too fast runaway of the neutron-capture reaction flow in this mass region. This is due to too strong shell effects of the $N = 82$ neutron shell closure, suggesting incomplete nuclear mass extrapolations to the nuclei with $Z \approx 40$ and $N \approx 70$–80, which correspond to the depleted abundance mass region $A \approx 120$. It is an interesting suggestion among many others (Woosley et al. 1994) that an artificial smoothing of the extrapolated zigzag structure of nuclear masses could fill the abundance dip around $A \approx 120$. This suggestion sheds light on the improvement of mass formula.

Let us repeat again that overall success in the present r-process nucleosynthesis calculation, except for several unsatisfactory fine features mentioned above, is achieved only for heavier mass elements, $130 \lesssim A$, including the second ($A \approx 130$) and the third ($A \approx 195$) peaks. From the disagreement of the abundance yields around the first ($A \approx 80$) peak relative to those at the third peak between our calculated result and the solar system r-process abundances, it is clear that a single-wind model is unable to reproduce all three r-process abundance peaks. The first peak elements should be produced under different conditions, with lower neutron-to-seed ratios and higher neutrino fluxes. It has already been pointed out by several authors (Seeger, Fowler, & Clayton 1965; Kodama & Takahashi 1975; Hillebrandt, Takahashi, & Kodama 1976) that even r-process nucleosynthesis needs different neutron exposures, as does s-process nucleosynthesis, in order to explain the solar system r-process abundance distribution. In a single supernova explosion event, there are several different hydrodynamic conditions in different mass shells of the neutrino-driven wind (Woosley et al. 1994; Witti et al. 1994), which may produce the first peak elements. Supernovae of different progenitor masses or events like exploding accretion disks in neutron-star mergers might contribute to the production of the r-process elements. Consideration of these possibilities is beyond our scope in the present paper.

We did not include the effects of neutrino absorption and scattering during the nucleosynthesis process in the present calculation (McLaughlin, Fuller, & Wilson 1996). This is because these effects do not drastically change the final r-process yields as long as the dynamic expansion timescale $\tau_{\rm dyn}$ is very short. Using equation (39), we can estimate the specific collision time for neutrino-nucleus interaction to be

$$\tau_\nu \approx 0.082\text{–}0.31 \text{ s} , \quad (43)$$

where the input parameters are set equal to $L_{\nu,51} = 10$, $\epsilon_\nu = 15$ MeV, and $\langle \sigma_\nu \rangle = 10^{-41}$ cm^2. Note that $\tau_\nu \approx 0.082$ s is the specific neutrino collision time at $r = 52$ km, where the temperature of the wind becomes $T = 0.5$ MeV at the beginning of the α-process, and $\tau_\nu \approx 0.31$ s for $r = 101$ km and $T = 0.5/e \approx 0.2$ MeV at the beginning of the r-process. These τ_ν values are larger than $\tau_{\rm dyn} = 0.0062$ s, which by definition represents the duration of the α-process. Therefore, the neutrino process does not disturb the hydrodynamic condition of rapid expansion during the α-process.

It is to be noted, however, that the neutrino process is almost entirely responsible for the slow expansion winds on the r-process. We have numerically examined the Woosley et al. (1994) model of trajectory 40 to find $\tau_{\rm dyn} \approx 0.3$ s. Meyer, McLaughlin, & Fuller (1998) also used $\tau_{\rm dyn} = 0.3$ s in their simplified fluid trajectory to investigate the neutrino-capture effects. This dynamic timescale $\tau_{\rm dyn} \approx 0.3$ s is larger than or comparable to the specific neutrino collision time τ_ν in equation (43). In such a slow expansion, neutrino absorption by a neutron (6) proceeds to make a new proton in the α-process. This proton is quickly interconverted into an alpha particle in the following reaction chain, $p(n, \gamma)d(n, \gamma)t$, which is followed by $t(p, n)^3\mathrm{He}(n, \gamma)^4\mathrm{He}$ and $t(t, 2n)^4\mathrm{He}$, and contributes to the production of seed elements. These radiative capture reactions and nuclear reactions are much faster than the weak process (eq. [7]) on a newly produced proton from the process in equation (6). The net effect of these neutrino processes, therefore, is to decrease the neutron number density and to increase the seed abundance, which leads to an extremely low n/s ratio. As a result, even the second abundance ($A \approx 130$) peak of the r-process elements disappears, as reported in literature (Meyer et al. 1998; Meyer 1995). Details on the neutrino process will be reported elsewhere.

We have assumed that electrons and positrons are fully relativistic throughout the nucleosynthesis process. However, the total entropy of the system may change at the temperature $T \lesssim 1/3m_e$, at which electrons and positrons tend to behave as nonrelativistic particles. This might affect nucleosynthesis, although it does not significantly affect the dynamics near the proto–neutron star. We should correct this assumption in future papers.

Finally, let us refer to a massive neutron star. Large dispersion in the heavy-element abundances of halo stars has recently been observed. Ishimaru & Wanajo (1999) have shown in their Galactic chemical evolution model that if r-process nucleosynthesis occurs in either massive supernovae, $\geq 30\ M_\odot$, or low-mass supernovae, 8–10 $M_\odot$, where these masses are for the progenitors, the observed large dispersion can be well explained theoretically. In addition, SN 1994W and SN 1997D are presumed to be due to 25–40 $M_\odot$ massive progenitors because of the very low ^{56}Ni abundance in the ejecta (Sollerman, Cumming, & Lundqvist 1998; Turatto et al. 1998). These massive supernova are known to have massive iron cores $\geq 1.8\ M_\odot$ and leave massive remnants (Turatto et al. 1998). Whether the remnant is a neutron star or a black hole is critical for r-process nucleosynthesis. Recent theoretical studies of the equation of state of neutron star matter, which is based on relativistic mean field theory, set the upper limit of the neutron star mass at $2.2\ M_\odot$ (Shen et al. 1998).

5. CONCLUSION AND DISCUSSIONS

We studied the general relativistic effects on neutrino-driven wind that is presumed to be the most promising site for r-process nucleosynthesis. We assumed spherically symmetric, steady state flow of the wind. In solving the basic equations for a relativistic fluid in the Schwarzschild geometry, we did not use an approximate method, as was adopted in several previous studies. We tried to extract generic properties of the wind in manners independent of supernova models or neutron-star cooling models.

General relativistic effects introduce several corrections to the equations of the motion of the fluid and also to the formula for the neutrino heating rate because of redshift and bending of the neutrino trajectory. We found that these corrections increase the entropy and decrease the dynamic timescale of the expanding neutrino-driven wind relative to those in the Newtonian case. The most important of these corrections proves to be the correction to the hydrodynamic equations. As distance increases without a remark-

able change of the velocity at $r < 30$ km, where neutrino-heating takes place efficiently, both the temperature and density of the relativistic wind decrease more rapidly than in the Newtonian wind. The lower the temperature and density are, the larger the net heating rate is. This is the main reason that the entropy in the relativistic case is larger than in the Newtonian case.

We also looked for suitable environmental conditions for r-process nucleosynthesis in the general relativistic framework. We first studied the differences and similarities between the relativistic and Newtonian winds in numerical calculations and then tried to interpret their behavior by expressing gradients of the temperature, velocity, and density of the system analytically under reasonable approximations. We extensively studied the key quantities for the nucleosynthesis, i.e., the entropy S and the dynamic timescale $\tau_{\rm dyn}$ of the expanding neutrino-driven wind, and their dependence on the proto–neutron star mass, radius, and neutrino luminosity. We found that more massive or equivalently more compact neutron stars tend to produce explosive neutrino-driven winds of shorter dynamic timescale, which is completely different from the result of the previous studies in the Newtonian case, which adopted approximation methods. We also found that the entropy becomes larger as the neutron star mass becomes larger. Since the larger luminosity makes the dynamic timescale shorter, the large neutrino luminosity is desirable as long as it is less than 10^{52} ergs s^{-1}. If it exceeds 10^{52} ergs s^{-1}, only the mass outflow rate becomes large and the flow cannot cool down to $\sim$0.2 MeV by the time it reaches the shock front at $r \sim 10{,}000$ km. As the result, the timescale becomes too long to be favorable for r-process nucleosynthesis.

Although we could not find a model that produces very large entropy, $S \sim 400$ as suggested by Woosley et al. (1994), this does not mean that the r-process does not occur in the neutrino-driven wind. We compared our results with Hoffman's condition and found that the short dynamic timescale $\tau_{\rm dyn} \sim 6$ ms, with $M = 2.0\,M_\odot$ and $L_\nu = 10^{52}$ ergs s^{-1}, is one of the most preferable conditions for producing r-process elements around the third peak ($A \sim 195$). In order to confirm this, we carried out numerical calculations of r-process nucleosynthesis with this condition by using a fully implicit single network code that takes account of more than $\sim$3000 isotopes and their associated nuclear reactions in a large network. We found that the r-process elements around $A \sim 195$ and even the heavier elements like thorium can be produced in this wind, although it has low entropy, $S \sim 130$. The short dynamic timescale $\tau_{\rm dyn} \sim 6$ ms was found to cause few seed nuclei to be produced with plenty of free neutrons left over at the beginning of the r-process. For this reason the resultant neutron-to-seed ratio, $n/s \sim 100$, in high enough even with low entropy and leads to appreciable production of r-process elements around the second($A \approx 130$) and third ($A \approx 195$) abundance peaks and even the hill of rare earth elements between the peaks.

Note that the energy release by the interconversion of nucleons into α-particles at $T \sim 0.5$ MeV produces an additional entropy, about $\Delta S \sim 14$. This was not included in our present calculation. We note that, including this increase, the r-process could occur in the neutrino-driven wind from a hot neutron star whose mass is smaller than $2.0\,M_\odot$.

One might think that short $\tau_{\rm dyn}$ brings deficiency of neutrino heating and that the wind may not blow. It is not true because the mass elements in the wind are heated by energetic neutrinos most efficiently at $r \lesssim 30$ km, while the expansion timescale $\tau_{\rm dyn}$ is the time for the temperature to decrease from $T \sim 0.5$ MeV to 0.2 MeV at larger radii. The duration of time for the mass elements to reach 30 km after leaving neutron star surface is longer than $\tau_{\rm dyn}$. There is enough time for the system to be heated by neutrinos even for $\tau_{\rm dyn}$ as low as $\sim$6 ms.

We did not include neutrino-capture reactions that may change Y_e during the nucleosynthesis process. Since the initial electron fraction was taken to be relatively high $Y_e = \sim 0.4$–0.5, there is a possibility that the final nucleosynthesis yields in neutrino-driven wind may be modified by the change in Y_e during the α- and r-processes. However, this is expected to make a small modification in our present expansion model with short dynamic timescale because the typical timescale of neutrino interaction is longer than $\tau_{\rm dyn}$. We will report the details about the nucleosynthesis calculation including neutrino-capture reactions in forthcoming papers.

It was found that the entropy decreases with increasing neutrino luminosity. This fact suggests that one cannot obtain large entropy by merely making the heating rate large. The cooling rate, on the other hand, does not depend on the neutrino luminosity. In the present studies we included two cooling mechanisms of the e^+e^- capture by free nucleons and the e^+e^- pair annihilation. As for the cooling rate due to the e^+e^- pair annihilation, only the contribution from pair-neutrino process is usually taken into consideration, as in the present calculation. However, there are many other processes that can contribute to the total cooling rate. They are the photo-neutrino process, the plasma-neutrino process, the bremsstrahlung-neutrino process and the recombination-neutrino process (Itoh, Hayashi, & Nishikawa 1995). Indeed, if we double our adopted cooling rate artificially, we can obtain larger entropy. Details on the numerical studies of the cooling rate are reported elsewhere. The radial dependence and general relativistic effect of the heating rate are also important (Qian & Woosley 1996 and Salmonson & Wilson 1999). Since both heating and cooling processes are critical in determining the entropy, more investigation on the neutrino process is desirable.

There are other effects that have not been included in the present study. They are, for example, the mass accretion onto the neutron star, the time variation of the neutrino luminosity, convection and mixing of materials, and rotation or other dynamic process that break the spherical symmetry of the system. These probably important effects may make several modifications to the present result. However, we believe that our main conclusion that there is a possibility of finding r-process nucleosynthesis in an environment of relatively small entropy and short dynamic timescale is still valid. We conclude that the neutrino-driven wind is a promising astrophysical site for successful r-process nucleosynthesis.

We are grateful to G. J. Mathews and J. Wilson for many useful discussions and kind advice. We also would like to thank R. N. Boyd, S. E. Woosley, H. Toki, K. Sumiyoshi, S. Yamada, and H. Suzuki for their stimulating discussions. This work has been supported in part by Grants-in-Aid for Scientific Research 1064236 and 10044103 from the Ministry of Education, Science, Sports, and Culture of Japan and the Japan Society for the Promotion of Science.

REFERENCES

Anders, E., & Grevesse, N. 1989, Geochim. Cosmochim. Acta, 53, 197
Bethe, H. A. 1990, Rev. Mod. Phys., 62, 801
———. 1993, ApJ, 412, 192
Bethe, H. A., Applegate, J. H., & Brown, G. E. 1980, ApJ, 241, 343
Bethe, H. A., & Wilson, J. R. 1985, ApJ, 295, 14
Burbidge, E. M., Burbudge, G. R., Fowler, W. A., & Hoyle, F. 1957, Rev. Mod. Phys., 29, 547
Burrows, A., & Mazurek, T. J. 1982, ApJ, 259, 330
Cardall, C. Y., & Fuller, G. 1997, ApJ, 486, L111
Cowan, J. J., Thielemann, F.-K., & Truran, J. W. 1991, Phys. Rep., 208, 267
Duncan, R., Shapiro, S. L., & Wasserman, I. 1986, ApJ, 309, 141
Hillebrandt, W. 1999, in Proc. International Symposium on Numerical Astrophysics 1998 (NAP98), ed. S. Miyama, T. Hanawa, & T. Tomisaka (Boston: Kluwer), 265
Hillebrandt, W., Takahashi, K., & Kodama, T. 1976, A&A, 52, 63
Hoffman, R. D., Woosley, S. E., & Qian, Y.-Z. 1997, ApJ, 482, 951
Ishimaru, Y., & Wanajo, S. 1999, ApJ, 511, L33
Itoh, N., Hayashi, H., & Nishikawa, A. 1995, AAS CD-ROM ser. 5 (Chicago: Univ. Chicago Press)
Käppeler, F., Beer, H., & Wisshak, K. 1989, Rep. Prog. Phys., 52, 945
Kodama, T., & Takahashi, K. 1975, Nucl. Phys. A, 239, 489
McLaughlin, G. C., Fuller, G. M., & Wilson, J. R. 1996, ApJ, 472, 440
Meyer, B. S. 1995, ApJ, 449, L55, Ph.D. thesis
Meyer, B. S., McLaughlin, G. C., & Fuller, G. M. 1998, Phys. Rev. C, 58, 3696
Meyer, B. S., Mathews, G. J., Howard, W. M., Woosley, S. E., & Hoffman, R. D. 1992, ApJ, 399, 656
Qian, Y. Z., Haxton, W. C., Langanke, K., & Vogel, P. 1997, Phys. Rev. C, 55, 1532
Qian, Y. Z., & Woosley, S. E. 1996, ApJ, 471, 331
Salmonson, J. D., & Wilson, J. R. 1999, ApJ, 517, 859
Seeger, P. A., Fowler, W. A., & Clayton, D. D. 1965, ApJS, 11, 121
Shapiro, S. L., & Teukolsky, S. A. 1983, in Black Holes, White Dwarfs, and Neutron Stars (New York: Wiley)
Shen, H., Toki, H., Oyamatsu, K., & Sumiyoshi, K. 1998, Nucl. Phys. A, 637, 435
Sneden, C., McWilliam, A., Preston, G., Cowan, J. J., Burris, D. L., & Armoski, B. J. 1996, ApJ, 467, 819
Sollerman, J., Cumming, R. J., & Lundqvist, P. 1998, ApJ, 493, 933
Sumiyoshi, K., Yamada, S., Suzuki, H., & Hillebrandt, W. 1998, A&A, 334, 159
Surman, R., Engel, J., Benett, J. R., & Meyer, B. S. 1997, Phys. Rev. Lett., 79, 1809
Symbalisty, E., & Schramm, D. 1982, Astrophys. Lett., 22, 143
Takahashi, K., & Janka, H.-Th. 1996, in Proc. Interntional Symposium on the Origin of Matter and the Evolution of Galaxies, ed. T. Kajino, S. Kubono, & Y. Yoshii (Singapore: World), 213
Takahashi, K., Witti, J., & Janka, H.-Th. 1994, A&A, 286, 857
Turatto, M., et al. 1998, ApJ, 498, L129
Witti, J., Janka, H.-Th., & Takahashi, K. 1994, A&A, 286, 842
Woosley, S. E., & Hoffman, R. D. 1992, ApJ, 395, 202
Woosley, S. E., Wilson, J. R., Mathews, G. J., Hoffman, R. D., & Meyer, B. S. 1994, ApJ, 433, 229
Woosley, W. E., & Weaver, T. A. 1993, in Les Houches Session LIV, ed. S. A. Bludman, R. Mochkovitch, & J. Zinn-Justin (Amsterdam: North Holland), 63
Wrean, P. R., Brune, C. R., & Kavanagh, R. W. 1994, Phys. Rev. C, 49, 1205
Yamada, S., Janka, T.-H., & Suzuki, H. 1999, A&A, 344, 533